https://doi.org/10.5194/egusphere-2026-4693
Preprint. Discussion started: 15 September 2026

Quantifying total methane emissions in the Permian Basin using MFIM: the MethaneSAT FLEXPART Inverse Model

Jacob B.H. Bushey[1], Michael Bertolacci[4], Joshua Benmmergui[1,2,3], Julian Kostinek[1], Maryann Sargent[1], Marvin Knapp[1,2], Ethan Kyzivat[1], Sasha Ayvazov[2,3], Marcus Russi[2,3], Zhan Zhang[1], Apisada Chulakadabba[5], Jia Chen[5], Christopher Chan Miller[1,2,6], Sébastien Roche[1,2,6], Lucas A. Estrada[1], James D. East[1], Luna Yin[1], James P. Williams[2], Anthony Himmelberger[2], Ritesh Gautam[2], Mark Omara[2] and Steven C. Wofsy[1]

[1]Harvard School of Engineering and Applied Sciences, 29 Oxford Street, Cambridge MA, USA
[2]Environmental Defense Fund, 257 Park Avenue S, New York NY, USA
[3]MethaneSAT LLC, 301 Congress Ave. Suite 1300, Austin TX, USA
[4]School of Physics, Mathematics and Computing, University of Western Australia, Australia
[5]Technical University of Munich, Professorship of Environmental Sensing and Modeling
[6]Center for Astrophysics | Harvard & Smithsonian, Cambridge, MA, USA

Correspondence to: Jacob B.H. Bushey (jbushey@g.harvard.edu)

Abstract. MethaneSAT was a spaceborne imaging spectrometer that observed column-averaged dry-air mole fractions of methane (XCH_4) in the atmosphere from March 2024 to June 2025. The data have fine spatial resolution (110 m x 400 m at nadir), high precision (~3 ppb at 2 km x 2 km aggregation) and wide swath (220 km at nadir). The goal of MethaneSAT is to provide comprehensive emissions characterization for oil and gas production regions, spanning the gap between area flux mappers and point source imagers. In this paper we introduce the MethaneSAT FLEXPART Inverse Model (MFIM), an inverse modeling framework for quantifying total emissions and their spatial distribution from MethaneSAT observations. We use a Lagrangian particle dispersion model, the FLEXible PARTicle dispersion model (FLEXPART v.11), in time reversed mode to determine the influence of surface emissions on atmospheric concentrations across a MethaneSAT scene (aggregated to 0.02° x 0.02° resolution). We then obtain the optimum emissions field using a Hamiltonian Monte Carlo (HMC) sampler to solve the inverse problem. We apply the inversion system to 9 scenes from the Permian Basin, yielding an annual emission rate of 3.49 ±1.43 Tg/yr (398 ±163 tons/hr). Emission estimates from MFIM resolve high emitting regions within the basin without the use of a spatially informed prior. MFIM leverages the strengths of the MethaneSAT observing system (10^4 independent observations) to produce spatially explicit, high-resolution (0.05° x 0.05°) emission estimates for application to monitoring and mitigation of methane emissions. Our results

https://doi.org/10.5194/egusphere-2026-4693
Preprint. Discussion started: 15 September 2026

compare well to the MethaneSAT Level 4 product from the operational CORE (Column Observations to Regional Emissions) inversion algorithm, as well as other top-down studies in the region, lending confidence that regional methane flux estimates from MethaneSAT are robust against differences in modeled transport.

1 Introduction

Emissions from the oil and gas (O&G) industry represent approximately 20% of the anthropogenic global methane budget (Saunois et al., 2025). O&G emissions represent the loss of a valuable commodity and largely arise from preventable processes and aging infrastructure. A comprehensive understanding of the emission sources, including accurate data on the location, rates and underlying processes that lead to emissions, would make it possible to adjust practices to avoid methane loss.

MethaneSAT was designed to provide data that enable us to determine methane emission rates for distinct (point) sources (Chulakadabba et al., 2023) and from dispersed (area) sources in O&G production regions. The sensor has fine spatial resolution (110 m x 400 m at nadir), high precision (~3 ppb at 2 km x 2 km aggregation) and a wide swath (220 km at nadir), enabling comprehensive emissions characterization. MethaneSAT observations are spatially and spectrally resolved, using sunlight reflected from the earth in two bands of the shortwave infrared (1248-1308 nm with 0.25 nm resolution and 0.08 nm sampling, and 1598 – 1683 nm with 0.3 nm resolution and 0.1 nm sampling). The MethaneSAT Level 2/Level 3 algorithms retrieve column densities of CO_2, CH_4 and O_2., and derive the dry air mole fraction (XCH_4) using the CO_2-proxy method as described by Chan Miller et al. (2024; 2026).

Here we introduce, evaluate, and apply the MethaneSAT FLEXPART Inverse Model (MFIM), a hierarchical inverse modeling framework for estimating basin-level emissions from MethaneSAT observations. We apply MFIM to estimate basin total methane emissions from the Permian Basin using high resolution data from MethaneSAT, determining both the basin total emission rate and the spatial distribution of emissions within the basin. The spatial distribution allows for a more targeted mitigation approach. We use the FLEXible PARTicle dispersion model (FLEXPART v. 11) (Bakels et al., 2024) to simulate atmospheric transport of methane in MFIM.

https://doi.org/10.5194/egusphere-2026-4693
Preprint. Discussion started: 15 September 2026

The framework builds on previous work using data from the MethaneAIR instrument (MacKay et al., 2025) and on the operational MethaneSAT data pipeline algorithm, Column Observations to Regional Emissions (CORE; MethaneSAT Science and Engineering Team, 2026). MFIM and CORE both do not depend on inventory-based priors for emissions quantification or spatial allocation, so that we can quantify new and/or transient sources wherever they may arise. Both models follow the same general framework, using the same observations, the same meteorological input, a time inverted Lagrangian transport model to relate concentrations to emissions and a Hamiltonian Monte Carlo (HMC) sampler. The MFIM framework differs from CORE in several important ways. Most important is the choice of transport model, but they also use different prior distribution assumptions and background estimation methods (Table 1). By highlighting similarities and differences between the MFIM and CORE algorithms we elucidate uncertainties associated with model structures and inputs. Comparisons between the models for both the total emission rate and the spatial allocation of emissions enable us to assess the uncertainties associated with using different transport models and other aspects of the modeling framework.

We apply MFIM to MethaneSAT observations of the Permian Basin (Fig. S1), a region that comprises a significant fraction (approximately 42% according to Zhang et al., 2020, Table S1) of the methane emissions from O&G basins in the continental United States. Previous studies of the region use both bottom-up and top-down methodologies to quantify methane emissions across spatial scales. The spatially Explicit Methane Emissions Inventory (EI-ME, Omara et al., 2024) and the Environmental Protection Agency's Greenhouse Gas Inventory (EPA GHGI, McDuffie et al. 2023) both use bottom-up methodologies. Top-down inversions have frequently used TROPOMI (TROPOspheric Monitoring Instrument) satellite observations to estimate Permian Basin emissions at resolution as small as 25 km as part of national (Shen et al., 2023; East et al., 2025; Estrada et al., 2026) and basin-specific studies (Zhang et al., 2020; Varon et al., 2023). Varon et al., (2023; 2026) showed that O&G emissions in the Permian Basin exhibit weekly variability and strong seasonality using weekly inversions of TROPOMI data and applying a Kalman Filter, a significant step towards near real-time emissions monitoring. However, the relatively sparse daily observation density and coarse pixel resolution of TROPOMI (5 x 7 km) limit the spatial resolution and temporal resolution of TROPOMI inversions. MethaneSAT observations provide the opportunity to push toward inversions with

https://doi.org/10.5194/egusphere-2026-4693
Preprint. Discussion started: 15 September 2026

higher spatial resolution that provide a snapshot of regional emissions for a single day as well as composites of the same region across several days.

We begin by introducing the data from 9 MethaneSAT scenes in the Permian Basin from 2024 and 2025. We then describe the inverse modeling framework. We examine how well the model recreates the observations (R^2 = 0.40-0.83, depending on the scene) and compare the spatial distribution of derived emissions between MFIM and CORE. We demonstrate that MFIM can use observations with high data density to produce single day emission estimates at high spatial resolution, quantifying distinct and dispersed sources simultaneously. By averaging emission estimates from 9 different data sets into a composite time-averaged estimate of 3.49 ±1.43 Tg/yr (398 ±163 tons/hr) we create an independent assessment of previously published bottom-up inventory results, which recovers the strong emitting regions within the Permian Basin without the use of a spatially informed prior. We compare the results to several previous studies in the region (Zhang et al., 2020; Shen et al., 2023; Veefkind et al., 2023; Varon et al., 2023; McDuffie et al., 2023; Omara et al., 2025; Varon et al., 2026; Williams et al., 2026; East et al., 2025; Scarpelli et al., 2025; Estrada et al., 2026). Comparison with bottom-up inventories and recent inverse modeling results for the Permian validates the MFIM inverse modeling framework for quantifying and spatially allocating emissions using MethaneSAT data.

https://doi.org/10.5194/egusphere-2026-4693
Preprint. Discussion started: 15 September 2026

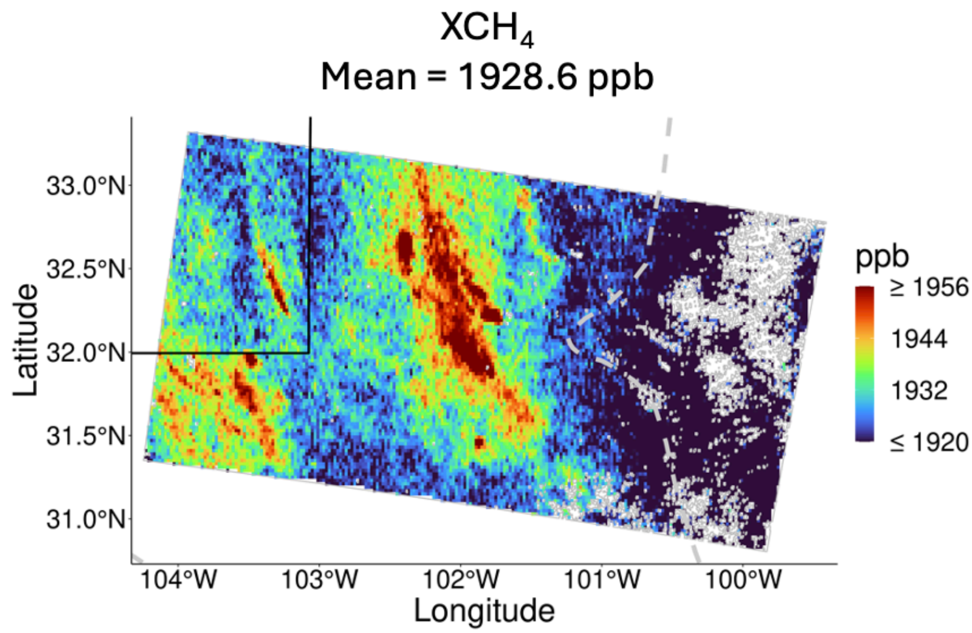

Figure 1. An example from 11 Sept., 2024 of total-column observations from MethaneSAT, smoothed with a Gaussian filter. The combination of resolution, precision and swath enable the simultaneous observation of both distinct and dispersed methane sources within the Permian Basin. Missing data (white) are due to clouds and data quality filtering. The solid black line shows the border between Texas and New Mexico. The dashed line shows the eastern boundary of the Permian Basin.

https://doi.org/10.5194/egusphere-2026-4693
Preprint. Discussion started: 15 September 2026

2 MethaneSAT Data

MethaneSAT measurements of the vertically averaged dry mole fraction of CH_4 (XCH_4) are obtained by retrieving the vertical column densities of CO_2 and CH_4 from reflected sunlight in bands centered at 1.61 and 1.64 µm, respectively, and taking their ratio (Staebell et al., 2021, Chan Miller et al., 2024). The proximity of the CH_4 and CO_2 measurement bands enables the CO_2-proxy method to quantify the column-averaged dry-air mole fractions of methane (XCH_4; Chan Miller et al., 2024) based on the assumption that the total column CO_2 concentration can be specified. This method has shown to perform better than "full-physics" approaches for other observing systems, as it is less sensitive to aerosol scattering and changes in albedo (Butz et al., 2010). Both priors (CH_4 and CO_2) used in the MethaneSAT CH_4 retrieval come from the GINPUT (Laughner et al., 2023) model developed for the Total Carbon Column Observing Network (TCCON) GGG2020 database (Chan Miller et al., 2024; Laughner et al., 2024). The oxygen $^1\Delta$ band is measured at 1.27 microns for cloud screening. De-striping, quality flagging and cloud screening are implemented as described in Chan Miller et al. (2026).

MethaneSAT was launched in March 2025 and collected data until June 2025, obtaining data for more than 70% of onshore oil and gas producing regions in the world. A MethaneSAT observation covers a region of approximately 200 km x 200 km at nadir, and up to 450 km x 200 km for off-nadir acquisitions. A single pixel at nadir is approximately 110 m across-track and 400 m along-track. We use the XCH_4 observations aggregated to 0.02° x 0.02° and smoothed with a Gaussian filter, giving single-pixel precision of ~3 ppb. Data filtering during aggregation removes outliers. For this analysis we will use data from observations made on 9 different days (hereafter referred to as scenes) over the Permian Basin, applying our inverse algorithm to each data set individually.

We will compare the MFIM inversion results to the operational MethaneSAT Level 4 product, CORE (MethaneSAT Science and Engineering Team, 2026). CORE is the production algorithm used for inversion of MethaneSAT data to obtain emissions maps.

3 Inverse Modeling Framework

Our inverse model has an $n \times 1$ state vector $\boldsymbol{x} = (x_1, \ldots, x_n)^T$ containing the unknown emissions on a 0.05° x 0.05° grid, and an $m \times 1$ observation vector $\boldsymbol{y} = (y_1, \ldots, y_m)^T$ containing observed

https://doi.org/10.5194/egusphere-2026-4693
Preprint. Discussion started: 15 September 2026

enhancements of methane column-integrated dry mole fraction, aggregated from native resolution to 0.02º x 0.02º. These vectors are related through

$$\boldsymbol{y} = \mathbf{K}\boldsymbol{x} + \boldsymbol{e}, \tag{1}$$

where $\mathbf{K}$ is an $m \times n$ Jacobian matrix representing the source-receptor relationship calculated using a transport model, and $\boldsymbol{e}$ is an $m \times 1$ vector of errors representing the mismatch between observations and modelled XCH_4. The (i, j)th entry of $\mathbf{K}$ is $\partial y_i / \partial x_i$, which can be interpreted as the expected change in XCH_4 at receptor i for a unit change in emission rate at location j.

To ensure positivity of the fluxes, we assign a zero-truncated multivariate Gaussian prior to $\boldsymbol{x}$ (see Michalak, 2008, though our computational approach differs). We assign a mean-zero multivariate Gaussian distribution to the errors, $\boldsymbol{e}$. The parameters both of the prior on $\boldsymbol{x}$ and the error distribution are considered unknown and are estimated as part of the inversion. Details on both distributions are given below. MFIM uses the FLEXPART Lagrangian particle transport model with 0.25º resolution winds from NOAA's Global Forecast System (GFS) to quantify the source-receptor relationship (Bakels et al., 2024). These are combined to compute the Jacobian matrix for the inverse problem.

The inverse framework is illustrated in Fig. 2. There are three major components (red rectangles) comprising three steps: Jacobian generation (subsection 1), data pre-processing (subsection 2) and emissions optimization (subsection 3). The first step constructs the Jacobian based on the output from the Lagrangian particle dispersion model (LPDM) FLEXPART. The second step selects MethaneSAT data that has passed the quality assurance and quality control (QA/QC) steps of data processing to remove irregularities in the data caused by clouds, cloud shadows, bodies of water, abrupt changes in albedo, spectroscopic artifacts and instrument drift. During this step we also aggregate the data to 0.02º x 0.02º resolution and discard any grid cells that contain < 50% valid data. This step takes the QA/QC data and applies a background model to remove methane from boundary inflow, leaving the XCH_4 enhancement traceable to emissions within the domain of interest. Step three uses a HMC algorithm, a Markov chain Monte Carlo method, to optimize the emission rates and calculate the basin total.

https://doi.org/10.5194/egusphere-2026-4693
Preprint. Discussion started: 15 September 2026

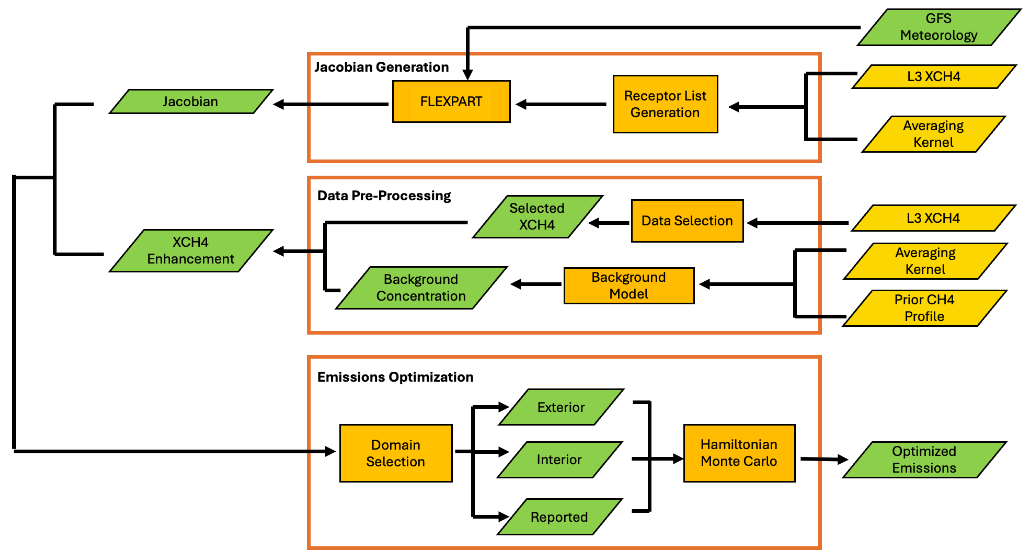

Figure 2. Schematic of the MFIM workflow for inference of methane emissions using MethaneSAT observations. The MFIM algorithm can be divided into three steps. First, it generates the Jacobian matrix using the FLEXPART LPDM with GFS meteorology. Second, it prepares the MethaneSAT Level 3 data for the inversion and uses this data to determine the topographic background for the region. Third, it uses the HMC algorithm to produce an optimal estimate of the spatially resolved emissions.

3.1 Jacobian Generation

By simulating the transport of air parcels throughout a vertical column of the atmosphere backwards in time and tracking their interactions with the surface FLEXPART establishes the relationship between emitters (sources) and total-column observations (receptors) contained in the Jacobian. The FLEXPART Lagrangian particle dispersion model (Bakels et al. 2024) is run in time-reversed mode so that each particle release can establish the footprint of surface influence on observations at that location (Fig. 3). Particle contact with the surface, which defines the footprint, is based on the residence time of the particle within the mixed layer, defined as the lower half of the planetary boundary layer (PBL). The PBL height is read from the GFS files used to run FLEXPART and interpolated from hourly resolution to the FLEXPART time stamps, which are at 5-minute resolution. The interpolation assumes that the boundary layer

https://doi.org/10.5194/egusphere-2026-4693
Preprint. Discussion started: 15 September 2026

grows and decays as a sigmoid function, beginning to grow at sunrise, reaching its peak at solar noon, and holding that peak until it decays rapidly at sunset. We resolve the FLEXPART output grid with vertical levels of 250m, 350m, 500m, 750m, 1000m, and 1500m, and round up from the mixed layer height to the nearest vertical level when defining the footprint.

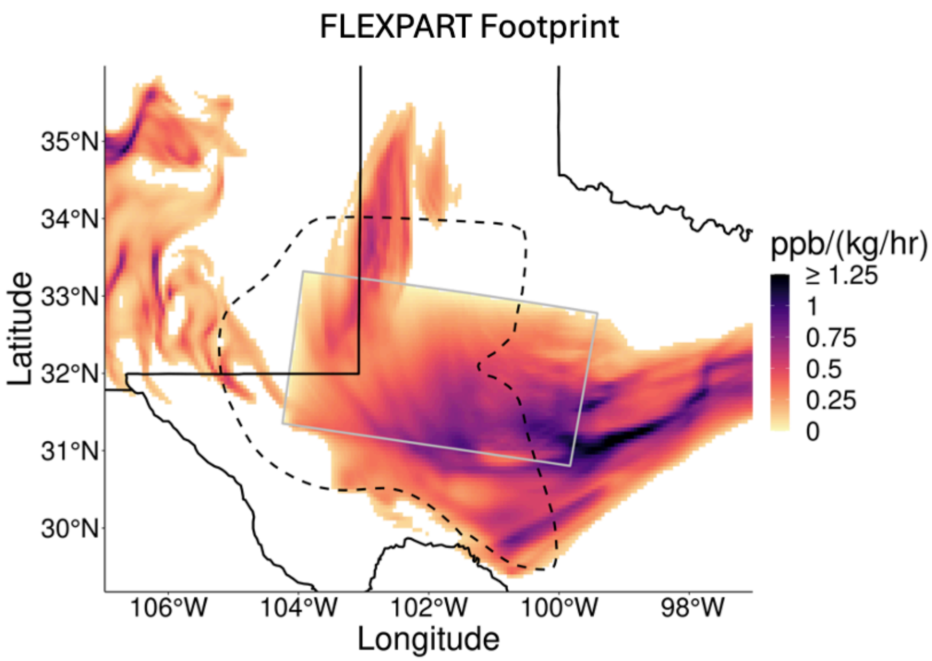

Figure 3. The influence footprint from all observations for MethaneSAT data collected on 11 Sept. 2024 shows that the prevailing wind direction produces a region of high influence to the east of the scene. This means that emissions in this region will have a larger influence on the concentrations in the scene. The grey outline shows the borders of the MethaneSAT data, the dashed black line outlines the Permian Basin, and the solid black lines depict the borders of Texas, New Mexico and Mexico. Portions of the footprint with a negligible influence on the observations are omitted.

Because we are simulating transport backwards in time from a total-column observation, it is necessary to account for the vertical sensitivity of MethaneSAT observations to each layer of the atmosphere. Each Level 2 retrieval has a unique averaging kernel, which represents the

https://doi.org/10.5194/egusphere-2026-4693
Preprint. Discussion started: 15 September 2026

sensitivity of the MSAT retrieval to 19 vertical layers in the atmosphere. We account for this sensitivity using an observation operator, which relates the modeled vertical column mixing ratios to the column-averaged dry-air mole fractions retrieved by MethaneSAT, allowing direct comparison of model output to observations. We apply the MethaneSAT averaging kernel as a weighting function on vertically distributed particle mass, interpolated to 55 vertical layers of particle releases within an atmospheric column in FLEXPART. This models the corresponding XCH_4 MethaneSAT would observe over the simulated atmosphere (Lauvaux and Davis, 2014; Hungershoefer et al., 2010; Eckhardt et al., 2008; Schneising et al., 2011; Zheng et al. 2019; O'Dell et al., 2012; Connor et al., 2008; Rodgers and Connor, 2003). The use of the observation operator informs our decision to run the transport model in time-reversed mode, because the observation operator can be applied to modeled particles at initialization, rather than applying it to the model output in post-processing.

We define a single averaging kernel for each MethaneSAT scene by taking the spatial average to create a scene-averaged averaging kernel, a simplifying assumption that captures the greater sensitivity of the retrieval to methane emissions at the surface. This assumption is acceptable for a region like the Permian Basin, which has relatively uniform albedo throughout the scene. Scenes with variable albedo may require a more careful treatment of the averaging kernel. Studies have shown that errors in the averaging kernel are negligible compared to transport errors and instrument noise (Li et al., 2022; Connor et al., 2008; Cogan et al., 2012; Zheng et al., 2019), so we neglect the contribution of the averaging kernel to the uncertainty in our treatment of the basin total emission rate uncertainty. A more detailed description of the averaging kernel incorporation into the model can be found in Appendix B.

FLEXPART is run for 36 hours backwards in time to give particles sufficient time to exit the observed domain and establish a footprint in outlying regions that can be used to optimize the boundary inflow to the region. We do not model chemistry because we assume that methane sinks are negligible over the 36-hour basin ventilation timescale (Hungershoefer et al., 2010).

3.2 Data pre-processing

We quantify and report emissions that originate within the domain, since the data contain insufficient information on emissions that originate upwind of the domain. To remove bias from methane sources outside of the domain, we need to remove the methane from each scene that

https://doi.org/10.5194/egusphere-2026-4693
Preprint. Discussion started: 15 September 2026

flowed into the domain from the exterior, leaving the enhancement in methane due to emissions within the domain. The modeled inflow has three components: (a) spatial variation accounted for by the XCH_4 prior used in the MethaneSAT retrieval algorithm, which is designed to explicitly avoid dependence on inventories (Laughner et al., 2023), (b) a constant synoptic-scale methane concentration, and (c) enhancements to inflowing air due to sources outside our observed domain. (a) includes, in order of importance, the mixing ratio variability due to topographic effects, the effect of the averaging kernel, and the latitudinal gradient of methane within a domain associated with global mean distributions. We remove the effects of topography on column-averaged dry-air mole fraction methane concentrations by correcting for the surface pressure dependence of the retrievals using the averaging kernel and Level 2 XCH_4 prior (MethaneSAT Science and Engineering Team, 2026. The synoptic scale mean for the background can be derived from the lower extremes of the observed XCH_4. We find this mean by shifting the XCH_4 variation due to topography such that it intersects with the lower extremes of our observations. We allow for small negative enhancements distributed as a half-Gaussian with a standard deviation equivalent to the instrument noise. This gives us the linear offset (c) that is scaled by the column-weighted Level 2 averaging kernel (**A**), according to Eq. 2 (MethaneSAT Science and Engineering Team, 2026).

$$\mathbf{y_{bg}} = \mathbf{y_{prior}} + c\mathbf{A}, \tag{2}$$

Where $\mathbf{y_{bg}}$ is the background XCH_4 and $\mathbf{y_{prior}}$ is the a priori XCH_4. The choice of the background is one of the largest potential sources of error when estimating the basin total emission rate, as it directly controls the basin total mass enhancement. An overestimate in the background will cause an underestimate in the mass enhancement, and thus the associated emissions, and vice versa. This approach presents the best estimate of the inflow in the presence of emissions near to, but outside of, the scene collected by MethaneSAT. There are other methods in the literature for determining the mean background, such as using a fixed percentile of the data (Lin et al., 2023), using observations from an upwind region (Tomlin et al., 2023; Schneising et al., 2020), or modeling and removing the contribution of methane above the boundary layer (Liu et al., 2021). Our method takes advantage of the information content of our data set to derive a background from a spatially complicated domain over a spatial scale where mesoscale and topographic

https://doi.org/10.5194/egusphere-2026-4693
Preprint. Discussion started: 15 September 2026

variability would make a single background value inappropriate. It also gives us the opportunity to identify an acceptable ensemble of mean-background-values which can be used to generate an error estimate on the basin total emissions (He et al., 2024). To account for the uncertainty of this method in our results, we run sensitivity inversions where the background is changed by ±2 ppb, a conservative error estimate considering the ~3 ppb single-pixel precision at 2 km x 2 km aggregation. This produces error of approximately ±15% in our emissions estimate.

We also consider observed variability due to emissions outside of our domain (Shen et al., 2021). We do this by optimizing buffer elements in addition to emissions within the domain, which account for both mesoscale variations in methane and near-field emissions immediately outside of the domain. Figure S13 shows an example of a MethaneSAT scene, with the domain outlined in grey and the surrounding buffer elements.

The buffer elements are clustered to a coarser spatial resolution than the emitters within the domain (see Subsection 3). Their emissions spread out as they are transported downwind into the domain. The choice to cluster the buffer elements in this way means that their emissions model low-frequency variations in the concentration field that propagate from the upwind boundary. This method for modeling boundary inflow effectively acts as a high-pass filter on the observations, separating the high-frequency variation due to local emissions from the low-frequency variation due to boundary inflow. After the background and boundary inflow have been removed, the enhancement that remains is attributable to local emissions, both distinct and dispersed sources.

3.3 Emissions prior and optimization

Following Stell et al. (2022) and Bertolacci et al. (2022), to the emissions $\boldsymbol{x}$ we assign the prior $N_{+}(\boldsymbol{x}_0, \boldsymbol{S}_0)$, the multivariate Gaussian distribution truncated to the positive orthant with mean vector $\boldsymbol{x}_0$ and covariance matrix $\boldsymbol{S}_0$. This ensures that the estimated emissions are positive. The mean vector is set to a constant rather than setting it equal to a spatially varying bottom-up estimate, so that our prior is uninformed with respect the spatial distribution of emissions. The covariance matrix is set to $\mathbf{S}_0 = \sigma_0^2 \mathbf{I}_n$, where σ_0^2 is the (unknown) prior variance and $\mathbf{I}_\mathrm{n}$ is the $n \times n$ diagonal matrix; thus we do not assume any correlation between emitters. We optimize emitters inside and outside of the domain simultaneously, in both cases assuming a Gaussian prior distribution truncated at zero. The emitters outside of the domain are grouped according to

https://doi.org/10.5194/egusphere-2026-4693
Preprint. Discussion started: 15 September 2026

their influence on the concentration field, using K-means clustering by cosine distance of the columns of the Jacobian matrix, which represent the transport footprints (Fig. S13). The clustering enables computational savings. By simultaneously optimizing the buffer elements and emissions within the domain, the buffer elements are less likely to overfit the data than they would be if we optimized them separately.

Similarly, we assume that the error vector $\boldsymbol{e}$ is multivariate Gaussian with mean zero and covariance matrix $\mathbf{S}_e = \sigma_e^2 \mathbf{C}_e$, where σ_e^2 is the (unknown) error variance (the model-data mismatch, effectively the sum of the transport and observation error) and $\mathbf{C}_e$ is a correlation matrix with exponential decay and an e-folding length of 1 km; the resolution of the observations is ~2 km x ~ 2 km, so this is a modest spatial correlation. Rather than fix σ_0^2 and σ_e^2 as is common practice, we follow Ganesan et al. (2014) by assigning priors to them and estimating their values as part of the inversion; details are given below and in Appendix A.

We use a Gibbs sampler to estimate emissions $\boldsymbol{x}$ and the unknown parameters σ_0^2 and σ_e^2. This involves iteratively sampling the conditional distributions of each variable, ultimately producing joint samples $(\boldsymbol{x}, \sigma_0^2, \sigma_e^2)$ from their posterior distribution. The steps for σ_0^2 and σ_e^2 are standard and are described in Appendix A, but for $\boldsymbol{x}$, which has a truncated Gaussian prior, we use the highly efficient HMC method proposed by Pakman and Paninski (2013), which was also used by Stell et al. (2022) and Bertolacci et al. (2022). The Gibbs sampler must be initialized to plausible values, run until it has converged to the target distribution (called the burn-in period, for which we use 100 samples), then run until the desired number of samples have been taken (only 400 samples are required due to the rapid convergence of the sampler). The optimized emissions are approximated by the mean of the samples of $\boldsymbol{x}$ after the burn-in period, and uncertainty estimates such as the posterior standard deviation can also be calculated from the samples. Estimating the full posterior distributions of σ_0^2 and σ_e^2 along with $\boldsymbol{x}$ has the advantage of making the inversion framework more adaptive to the data, and also of incorporating the uncertainty of these parameters into the fluxes (Ganesan et al., 2014). See Appendix A for a more thorough treatment of the sampler.

The above choices have the following benefits in the context of methane. Because we neglect methane sinks, our emission rates must be positive or zero, so enforcing non-negativity with the truncated normal distribution improves the interpretability of our results. The combined effect of the background selection method and the non-negativity constraint is the ability to model

https://doi.org/10.5194/egusphere-2026-4693
Preprint. Discussion started: 15 September 2026

physically realistic enhancements produced by positive emissions, at the cost of treating a small number of negative enhancements as model error.

The use of a spatially invariant prior mean over emitters instead of one based on inventories lets the system take advantage of MethaneSAT's unique combination of spatial and spectral capabilities through which it should be able to observe emitters missed by other observing systems and inventories. Previous work has demonstrated this ability with the spectrally similar MethaneAIR instrument, observing a pipeline blowout (Chan Miller et al., 2024). The CORE algorithm for MethaneSAT uses a different approach that incorporates a spatially informed prior and assumes a log-normal distribution of emitters (MethaneSAT Science and Engineering Team, 2026).

An improper spatial distribution in the prior can propagate as bias into posterior estimate. Instead, our posterior estimates are entirely guided by the MethaneSAT observations, which have sufficient data density to constrain the emissions. This method is particularly beneficial in oil and gas basins where rapid development, strong variability, and one-off emission events can cause strong discrepancies in prior inventories (Varon et al., 2026). The emission estimates are not sensitive to the choice of the prior mean.

4 Emission Rates

Within each sample, we sum across all emitters to produce a sample of the domain total emission rate; we then summarize these samples by taking the mean. The basin totals for each scene are given in Fig. 6 and Table S1. We give results for both the mean and the median in Table S3 to demonstrate that the result is not sensitive to our choice of metric, demonstrating that the model avoids potential bias associated with our adoption of a positive definite distribution of emissions (Michalak et al., 2008). Subtracting the sum of the point source emission rates, quantified according to Chulakadabba et al. (2023) from the basin total gives us emissions due to diffuse area sources. The relative contribution of the distinct sources to the basin total for each observation is given in Fig. C1 and Table S2.

5 Box Model

As a first-order comparison to the results of our inversion, we use a simple box-model that approximates the methane emission rate using the lifetime of methane in the domain.

https://doi.org/10.5194/egusphere-2026-4693
Preprint. Discussion started: 15 September 2026

$$Emissions = \frac{M}{\tau}, \tag{3}$$

Where M is the total mass of methane in the domain and τ is the flushing time of the domain. We use the average XCH_4 enhancement from each inversion and convert it to a total mass enhancement using the assumption of a standard atmosphere. We approximate the flushing time of the domain by dividing the domain length scale by the average wind speed from GFS between the surface and 1500 m. The domain length scale is the average distance a parcel of air containing methane would have to traverse to exit the scene, approximated by the radius of a circle with the same total area as the domain.

https://doi.org/10.5194/egusphere-2026-4693
Preprint. Discussion started: 15 September 2026

6 Results and Discussions

A comparison of the posterior XCH_4, found by taking the mean of the proposed samples, and the observations shows that the data are well-correlated (Fig. 4a). The R^2 of the regression tells us how effectively the model was able to reproduce the observations ($R^2 = 0.40$-0.83, depending on the scene), which is a useful proxy for model performance in the face of imperfect meteorological data products. Figure 4b shows the histograms for the observations (blue) and posterior enhancements (orange). The non-negativity constraint creates a minimum enhancement that the model can produce, which leads to more enhancements near 0 ppb. The diffusivity of the transport model makes it difficult to reproduce the largest enhancements, leading to more enhancements near the middle of the distribution. The figures demonstrate good agreement between the observations and the posterior, with discrepancies due to expected model behavior.

https://doi.org/10.5194/egusphere-2026-4693
Preprint. Discussion started: 15 September 2026

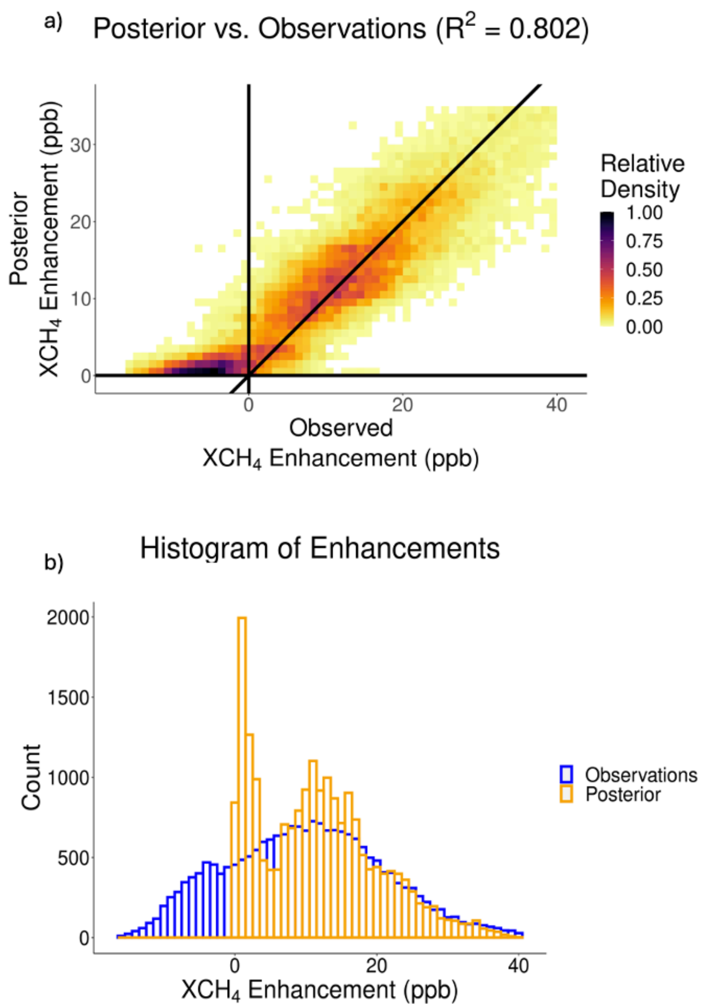

Figure 4. (a) A binned scatterplot of the posterior enhancements compared to observations for data collected on 11 Sept. 2024. The black line is the 1:1 line. (b) A histogram of the observations (blue) and modeled concentrations (orange). These figures for each of the 9 domains can be found in Figures S1-S9.

Figure 5 shows an example map of the residuals between the observations and modeled concentrations. The residual plots do not tell us how accurate our spatial distribution is, since a perfect match would indicate an overfit. They do however give us a qualitative understanding of

https://doi.org/10.5194/egusphere-2026-4693
Preprint. Discussion started: 15 September 2026

the scale at which the transport models will have difficulty accurately represent atmospheric processes, because the observations are at much higher resolution than the meteorological product used to drive the transport model.

There are two main contributions to the spatial discrepancy shown in the residual map. The first is that the background estimation method allows for small negative enhancements that the model cannot reproduce. These dominate the eastern side of the map in Fig. 5, in part because of cloud cover in the region. Throughout the rest of the figure, the spatial discrepancy is largely due to wind errors in the transport model used to construct the Jacobian at such high resolution (He et al., 2024; Zheng et al., 2019). We will refer to the combination of errors in the meteorological data product and the transport model as model error. Discrepancies in transport between different models (Munassar et al., 2023; Schuh et al., 2019) and between any model and reality (Zheng et al., 2019) are well documented. Even as the resolution of observations continue to improve, higher resolution inversions will not necessarily be more accurate due to model error (Deng et al., 2017). Compensating spatial errors tend to cause inversions to be more accurate at large spatial scales, especially when observations are collocated with sources as they are for MethaneSAT data (Deng et al., 2014; Locatelli et al., 2013; Basu et al., 2018; Houweling et al., 2010; Lauvaux and Davis, 2014).

The model error has a greater impact on the spatial allocation of emissions than the basin total. The magnitude is difficult to assess, as we have no ground truth meteorological data or emission rates with which to compare our transport and inversion results. While we are unlikely to have a controlled release experiment on the scale of an entire basin to act as ground-truth for inversion results, observations that are sufficiently dense in both space or time could dramatically increase confidence in inversion results and create a quasi-ground-truth data set to which more data-sparse inversion methods can be compared. In addition, developing more accurate high resolution wind models poses a significant hurdle to inverse modeling at this scale. A rigorous quantification of transport model error is treated elsewhere in the literature (Zheng et al., 2019; Locatelli et al., 2013; Basu et al., 2018; Houweling et al., 2010; Lauvaux and Davis, 2014) but is beyond the scope of this paper.

https://doi.org/10.5194/egusphere-2026-4693
Preprint. Discussion started: 15 September 2026

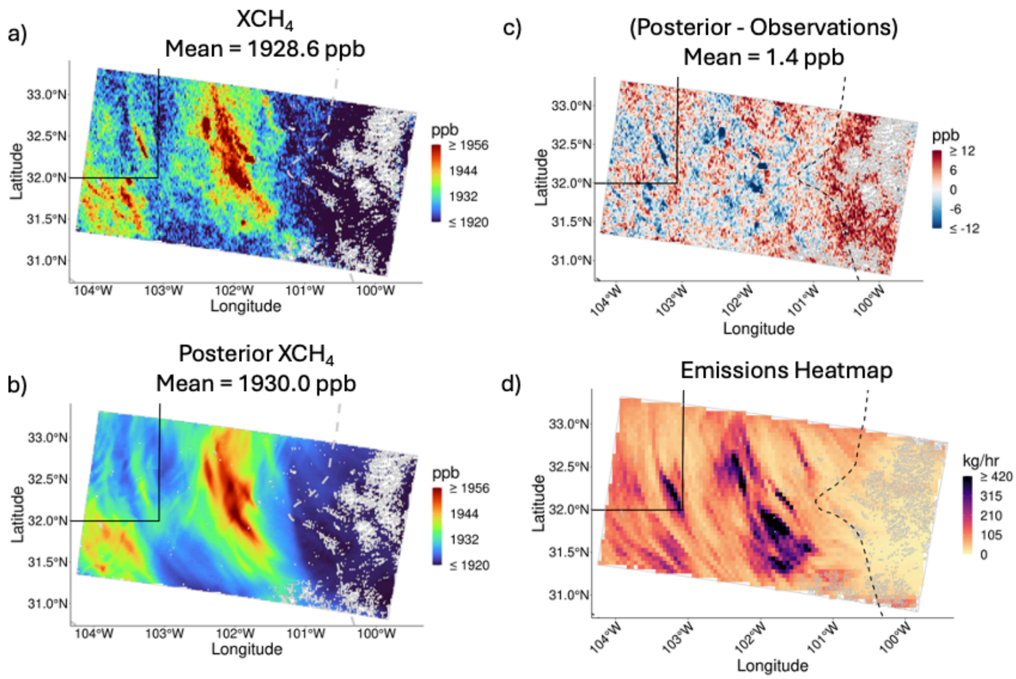

Figure 5. Data and model results from 11 Sept. 2024. (a) The total-column observations from MethaneSAT, smoothed with a Gaussian filter. (b) The posterior modeled concentrations produced by propagating the MFIM emissions forward in time through the Jacobian. (c) The residual between the observations and the posterior modeled concentrations has an average across the scene of approximately 1 ppb. (d) The emissions heatmap shows high emissions collocated with the observed enhancements in XCH_4. The solid black line shows the border between Texas and New Mexico. The dashed line shows the eastern boundary of the Permian Basin.

6.1 Basin total emission estimates

The results from MFIM for each of the 9 inversions are presented in Fig. 6. The error bars account for uncertainty in the background concentration by running sensitivity inversions with ±2 ppb background concentrations to determine the upper and lower bounds of the emissions estimate. Uncertainty in the HMC sampler itself is accounted for by using the 2.5th and 97.5th percentile estimates for the lower and upper bound, respectively. We add an additional ±20%

https://doi.org/10.5194/egusphere-2026-4693
Preprint. Discussion started: 15 September 2026

uncertainty to the basin total to account for uncertainty in the GFS wind product used in the inversion. We also show comparisons to results from CORE (MethaneSAT Science and
460 Engineering Team, 2026), the EI-ME (Omara et al., 2024), and the simple box model approach described above (listed as Mass in Fig. 6). Appendix D discusses a version of MFIM where the background has been adjusted such that the mean of the observed enhancement equals the mean of the posterior modeled enhancement from CORE, referred to as MFIM_adj. Spatially resolved emission estimates from MFIM for each data set are given in Figs. S1-S9.

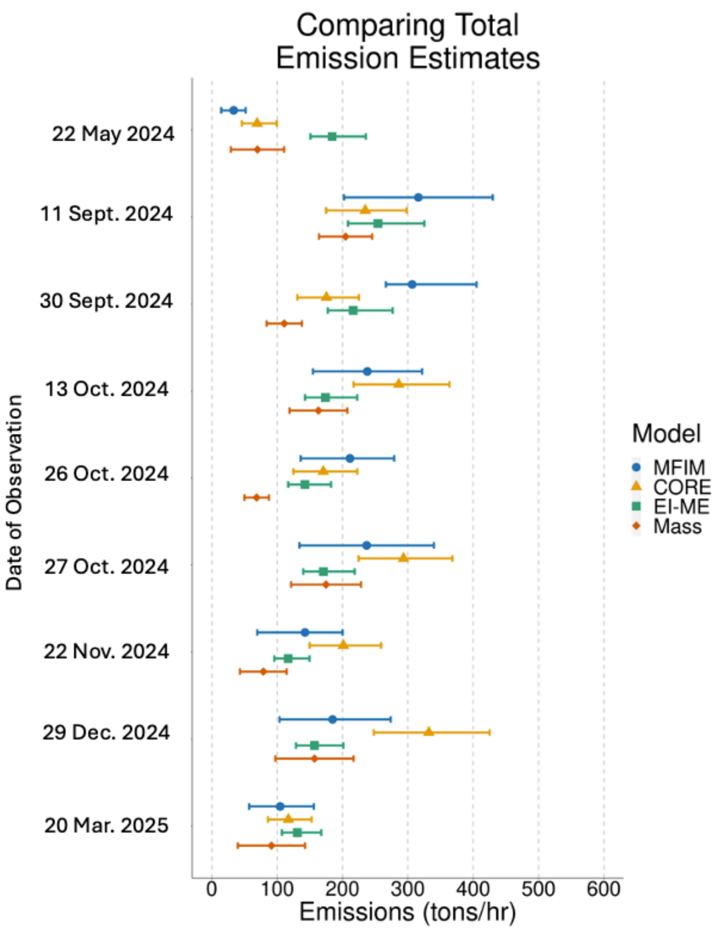

Figure 6. Comparison of results for all 9 scenes from the Permian Basin. The models include MFIM, operational CORE, the EI-ME and the mass balance approach. Error bars for this study

https://doi.org/10.5194/egusphere-2026-4693
Preprint. Discussion started: 15 September 2026

include the 2.5th and 97.5th percentile spread in the HMC sampler, sensitivity inversions of ±2 ppb in the background and an assumption of 20% error due to transport. Error estimates for the mass balance just factor in the ±2 ppb background sensitivity. Error bars for CORE (MethaneSAT Science and Engineering Team, 2026) give the 95% confidence interval. Error bars for the EI-ME (Omara et al., 2024) scale the given confidence interval (-18%, +28%) to the domain. Data for the EI-ME is from 2021.

The results from MFIM are higher than the EI-ME by an average of 14.2%. This is a reasonable level of agreement, especially in light of well documented discrepancies between bottom-up and top-down approaches (Saunois et al., 2016; Saunois et al., 2025; Allen, 2014; Vaughn et al., 2018; Zhao et al., 2023). The EI-ME reports annualized average emissions and discrepancies in total emissions may be explained by variations in emitter persistence and an incomplete representation of short-lived "super-emitter" emissions events by the EI-ME, which may cause the EI-ME to underestimate emissions in the region.

The results from MFIM are higher than the Mass model estimates by 64.7%. MFIM and Mass inter-model agreement can be quantified by the absolute value of the percent difference between their emission estimates, relative to the Mass model. We find a negative correlation between wind speed and inter-model agreement ($R^2 = 0.61$), showing that the largest discrepancies come from domains with low wind speeds. Low wind speeds increase the flushing time and cause emissions to be underestimated (Eq. 3). Complex wind fields are similarly likely to cause discrepancies between the models, since the Mass model contains no information about wind direction. We conclude that simple box models serve as reasonable first-order estimates of total emissions, but can underestimate by as much as a factor of 2.

Finally, we compare MFIM to results from the operational CORE algorithm. On average MFIM is lower than CORE by 4.3%, well within error estimates for both models. Discrepancies in the two models, both in basin totals and their spatial allocation, may arise from differences in transport models, optimization algorithm, background concentration specification and the choice of prior information. For transport, CORE uses the Stochastic Time-Inverted Lagrangian Transport Model (STILT) (Lin et al., 2003) while MFIM uses FLEXPART. Both are run in time-reversed mode, but STILT is run for 28 hours in CORE, while FLEXPART is run for 36 hours in MFIM. CORE assumes a lognormal prior distribution, while MFIM assumes a normal

https://doi.org/10.5194/egusphere-2026-4693
Preprint. Discussion started: 15 September 2026

distribution truncated at zero. The background concentrations are fixed in MFIM, while CORE allows the offset to shift as a part of the optimization. They use different implementations of the HMC sampler, with CORE using Stan (Carpenter et al., 2017) and MFIM using an R-based implementation. Finally, MFIM does not incorporate a spatially informed prior, while CORE uses global emission estimates from IMI 2.0 (East et al., 2025). The prior does not have a measurable impact on high emitting grid cells but regularizes the emission in low-emitting regions. Thus, emitter cells are constrained to posterior emissions smaller than the data alone can support. In CORE, this specifically supports constraining the background concentration during the inversion (MethaneSAT Science and Engineering Team, 2026).

	MFIM	**CORE**
Transport	FLEXPART	STILT
Prior Distribution	Normal truncated at 0	Lognormal
Background	Fixed	Fitted during optimization
HMC Sampler	R-based implementation	Stan
Spatially Informed Prior	None	IMI 2.0 (East et al., 2025)

Table 1. A summary of the differences between MFIM and CORE modeling frameworks, which explains the differences between the two models in basin total emissions and their spatial distribution.

For some data sets (ex. 27 Oct. 2024), the difference between MFIM and CORE is driven by differences in the background concentration. On other days (ex. 29 Dec. 2024) changing the background to align with CORE does not change the basin total for MFIM, and so the discrepancy is likely driven by differences in transport or other modeling assumptions (see Appendix D). Munassar et al. (2023) found a nearly 30% difference between inversions using these two transport models. These results fall well within that level of agreement. Maier et al. (2025) demonstrate that inversions using FLEXPART and STILT show only minor deviations when using the same meteorology under good observing conditions. Many of the scenes analyzed here support this conclusion, while others demonstrate the challenge of quantifying emissions on days when observing conditions are less than ideal.

https://doi.org/10.5194/egusphere-2026-4693
Preprint. Discussion started: 15 September 2026

By examining the scenes where CORE and MFIM have the greatest disagreement, we can improve our understanding about the limitations of each model. The correlation between MFIM and CORE inter-model agreement (the absolute value of the percent difference between their emission estimates) and the magnitude of distinct sources relative to the basin total ($R^2 = 0.27$) indicates that an increased relative contribution due to distinct sources causes greater disagreement between the two models because both perform worse when fitting observations under these conditions. The presence of a distinct source makes the accuracy of the transport models more consequential. Errors in meteorological data (wind speed and direction) are exacerbated by steep concentration gradients from distinct sources, which the models have difficulty reproducing. This makes it more difficult to minimize the cost function when optimizing concentrations, which can influence the basin total emission rate and exacerbate the differences the two transport models. The same dynamic can make it difficult to model large enhancements at the inflowing or outflowing edge of a scene. These challenging conditions highlight the strengths of the observing system itself but push the boundaries of the model capabilities and exacerbate known uncertainties in the models.

GFS meteorological data on 13 Oct. 2024 shows an apparent mismatch between the expected and observed wind directions in the target scene. This challenges the emission inversion; MethaneSAT refrains from releasing such scenes on their data portal. The scene is included here as the comparison to MFIM usefully illustrates the challenges with modeling emissions at this scale with imperfect meteorological data.

The MFIM and CORE modeling frameworks do not factor in source intermittence throughout the duration of the modeled transport (36 hours for MFIM, 28 hours for CORE), or the fact that the probability of detecting an emitter is not unity (Manninen et al., 2026), although these assumptions are more valid over the relatively short time frame of our inversion (hours to days) than over the timeframes of previous inverse analyses (weeks to months). Future studies should address the question of emitter transience using repeat observations within a single 24-hour window.

6.2 Time-Averaged Emissions

Figure 7 shows the combined emission estimates for each MethaneSAT scene by taking the average in regions where they overlap, giving us a time averaged emission estimate for the

https://doi.org/10.5194/egusphere-2026-4693
Preprint. Discussion started: 15 September 2026

Permian during the observation period. We see a clear spatial pattern emerge outlining the two sub-basins, the Midland and Delaware Basins. This gives us confidence that across many inversions errors in the spatial allocation tend to cancel each other out and reveal true average spatial patterns. The edges of the individual domains are visible in the composite, but this would become less significant as the number of repeat observations increases.

The basin total emission rate for this composite is 398 ±163 tons/hr. If we assume that this number sufficiently captures the temporal variability of emissions in the region and extrapolate out to an entire year, we get an emissions estimate of 3.49 ±1.43 Tg/yr. This is number is consistent with estimates from other studies of the Permian Basin (East et al., 2025; Estrada et al., 2026; Shen et al., 2023; Varon et al., 2023; Williams et al., 2026; Zhang et al., 2020) (Fig. 9). The EI-ME cropped over the same region has a total emission rate of 324 tons/hr. The MFIM composite is higher by 22.8% due to the incomplete representation of short duration emissions described previously, which causes the EI-ME to underestimate emissions in the region. Figure S11 shows that MFIM does a good job capturing the spatial variability present in the EI-ME, even though there is no prior information about spatial distribution in MFIM. Fine details in the residual plot reveal important differences between the two models. Several (red) hotspots appear in MFIM that are not found in the EI-ME. Similarly, the (blue) Central Basin region between the Delaware and Midland sub-basins shows that the EI-ME has high emissions in this region. These discrepancies are likely due to a combination of the smoothing effect of transport inherent in an inverse modeling framework, and the different prior distribution assumptions used by the models.

https://doi.org/10.5194/egusphere-2026-4693
Preprint. Discussion started: 15 September 2026

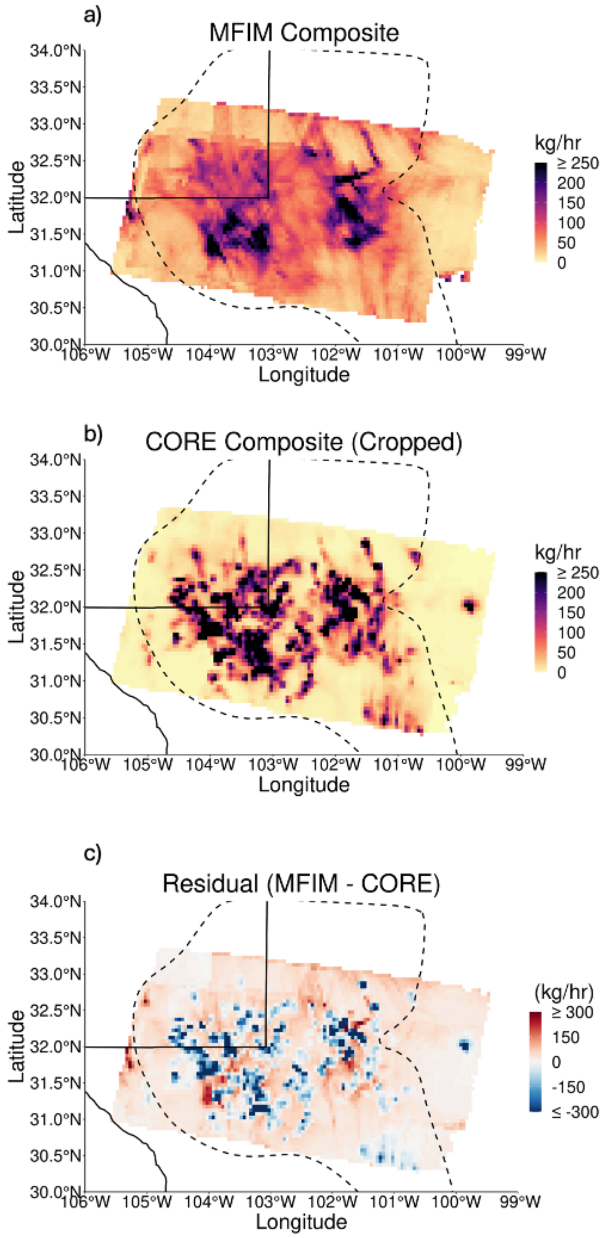

Figure 7. (a) composite of the emission estimates from all 9 scenes in the Permian basin using MFIM. The composite allows us to approximate the long-term average emission rate and the spatial distribution of those emissions. (b) The composite of the same 9 scenes using CORE,

https://doi.org/10.5194/egusphere-2026-4693
Preprint. Discussion started: 15 September 2026

resampled by averaging to the 0.05° x 0.05°. (c) the residual between the MFIM and CORE composites, which sheds light on the spatial uncertainty of the emission estimates.

The MFIM composite total emission rate is higher than the CORE composite by 8.7% over the same region. Note that the difference between the composites is not the same as the average of the differences for each scene (4.3% lower) because each scene covers a different spatial extent. The composite emission estimates from both models recover strong emitting regions in the Delaware and Midland sub basins. The fact that the models agree regardless of whether they incorporate information from a spatially informed prior demonstrates the strength of MethaneSAT observations for informing emission estimates.
Because they use the same data, but different transport models and different prior assumptions, comparing the spatial distributions of the two inversions can shed light on the modeling assumptions we employ and give an estimate on the spatial uncertainty of both models (He et al., 2024). We compare the spatial distributions of the MFIM and CORE composites in Fig. 7. The operational CORE inversion tends to produce posterior emissions with sharp gradients and much larger peaks in emissions, while MFIM tends to be smoother and have lower peaks. The peaks in the CORE emissions are indicative of distinct sources, showing up as (blue) hotspots on the residual plot. Another way to describe this difference is that for low emitting grid cells, MFIM tends to produce a higher estimate than CORE. For high emitting grid cells CORE tends to produce a higher estimate than MFIM. Figure 8 helps us to visualize this difference.
There are several possible explanations for this discrepancy. Most importantly, we see that regions of small, diffuse emissions in MFIM have near-zero emissions in CORE due to the regularizing effect of the prior. The assumption of a lognormal distribution in the operational CORE algorithm allows for much larger individual emitters, producing sharp gradients. Additionally, the transport in FLEXPART tends to be narrow relative to STILT, which has the effect of smoothing the emissions field. Other differences in transport, including how the boundary layer is represented, may also play a role.

https://doi.org/10.5194/egusphere-2026-4693
Preprint. Discussion started: 15 September 2026

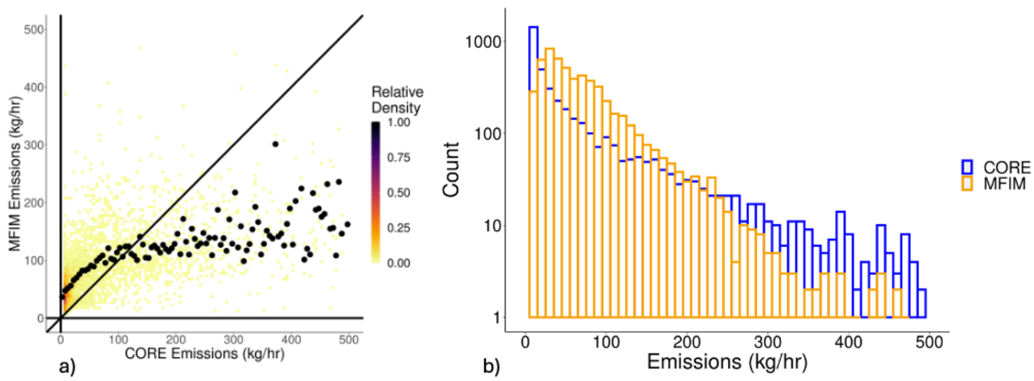

Figure 8. (a) A binned scatter plot comparing the emissions estimates for each cell of the MFIM and CORE composites. The black points give the bin-wise average for emitters, filtered for CORE emitters between 0 and 500 kg/hr for interpretability (which removes < 3% of each data set). (b) A histogram of the emissions estimates for each cell of the MFIM and CORE composites, plotted with the y-axis on a log-scale to make the fat-tail of the distribution distinguishable.

The spatial resolution of both inversions makes the data useful for analyzing both temporal and spatial trends in the data, like calculating differences in emission trends in different jurisdictions within a single basin (e.g. Williams et al., 2026). Future model development should focus on selecting a spatial scale for the inversion such that uncertainty in the spatial distribution of emissions is minimized, and on specifying which components of atmospheric transport contribute most to this discrepancy.

Figure 9 shows comparisons between the MFIM composite, CORE, the EI-ME and several other studies cropped over the same spatial extent. We see good agreement between these studies and inventories, except for Scarpelli et al. (2025) and the US EPA Greenhouse Gas Inventory (EPA-GHGI; McDuffie et al., 2023; Maasakkers et al., 2023) where we find emissions at a rate approximately 3 times higher than that reported to the EPA. This confirms the findings of other top-down studies using data from MethaneAIR (McKay et al., 2025) and MethaneSAT (Williams et al., 2026) and matches the general pattern that top-down methodologies find higher emission rates than bottom-up methodologies. The MFIM composite estimate falls within error bars for all of the most recent top-down inversions of the Permian — Varon et al. (2023), East et

https://doi.org/10.5194/egusphere-2026-4693
Preprint. Discussion started: 15 September 2026

al. (2025), Varon et al., (2026), Estrada et al. (2026, data available at https://laestrada.github.io/conus_emissions_viz/) and the operational CORE algorithm.

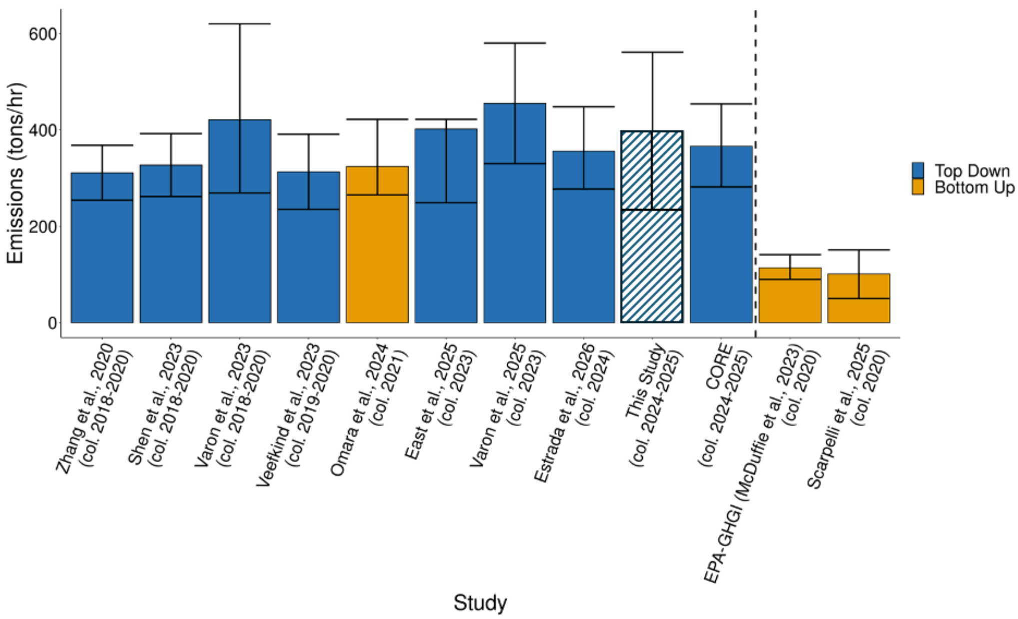

Figure 9. Basin total methane emissions from multiple studies for the region covered by the composite image shown above. Studies are listed in order of the year their data was collected, except for the much lower estimates from the bottom-up studies, which are separated by a dashed black line. Hatch marks are used to highlight the results from this study. We choose to group the data from the EI-ME with the top-down studies because it uses comprehensive oil and gas activity data and accounts for the fat-tail of the emissions distribution, producing results more akin to these studies than to other bottom-up estimates. Error bars for this study assume the average error of each of the individual inversions, ±41%. Gridded studies are cropped to the same region as the MFIM composite. Error bars for CORE scale the confidence interval (-23%, +24%) published in Williams et al. (2026), which covers approximately the same region of this study. Error bars for the EI-ME (Omara et al., 2024) scale the given confidence interval (-18%,

https://doi.org/10.5194/egusphere-2026-4693
Preprint. Discussion started: 15 September 2026

+28%) to the domain. The same approach is used for Estrada et al. (2026), with a confidence interval of (-22%, +26%). The error bars from Varon et al. (2023) use the 5^{th} and 95^{th} percentile of the weekly emission estimates cropped over the region. The error bars from Varon et al., (2026) scale the given confidence interval (4.0 ± 1.1 Tg a^{-1}) to the domain. The error bars for Shen et al. assume ±20%, which is comparable to the ±0.5 Tg/year given in Zhang et al. (2020). The error estimates from McDuffie et al. (2023) are the same as those given in the 2018 GHGI (Maasakkers et al., 2023), since no new error estimates are given for the 2020 express product. Error bars from Scarpelli et al. (2025) are 50%, which is the average of the relative standard deviation (RSD, %) from Scarpelli et al. (2020) for all oil and gas activities (Table 1).

https://doi.org/10.5194/egusphere-2026-4693
Preprint. Discussion started: 15 September 2026

7 Conclusion

We developed a new inverse modeling framework, MFIM, for quantifying basin total emission rates from oil and gas basins observed by MethaneSAT, a satellite with unique observing characteristics. We used this model to produce emission heatmaps for 9 independent data sets. Residual plots and regressions comparing the observations and the modeled concentrations show that the model effectively reproduces the observations. The composite of all 9 inversions gives an annual emission rate of 3.49 ±1.43 Tg/yr (398 ±163 tons/hr) from the Permian Basin, which agrees well with previous inversion results. The spatial distribution of the MFIM composite is comparable to the results from the operational MethaneSAT Level 4 product, CORE, and successfully resolves the Midland and Delaware sub-basins within the Permian while using a spatially invariant prior, giving us confidence in the spatial distribution.

By comparing the results of two inversions using the same observations and meteorological drivers but with different transport models and prior information assumptions, we have successfully cross-validated the methods for estimating dispersed methane sources. This method of validation is important since controlled release experiments are infeasible at this scale. Discrepancies between the two models are likely attributable to transport errors. Previous studies have discussed the need for meteorological and transport models to advance at the same pace as observing systems, as errors in wind speed and direction can cause uncertainty in the spatial allocation of inversions performed at high spatial resolution (Zheng et al., 2019). The results outlined here confirm that this challenge still faces the research community.

This study adds to the growing body of work applying FLEXPART to inverse modeling problems for methane emissions using satellite data (Thompson et al., 2025; Subramanian et al., 2025). The modeling framework described here is applicable to observations from other high-resolution platforms like CO2M (Sierk et al., 2021) and MethaneAIR (McKay et al., 2025), making observations over other oil and gas basins, as well as urban and agricultural regions. These results highlight the value of low-latency, high resolution emission estimates from MethaneSAT. The revisit time made it possible to collect repeat observations over a single location of interest and track changes in emission rates through time. Using just 9 days of MethaneSAT observations, we are able to confidently quantify emissions at a scale that would otherwise require months or years of spatially oversampled data from satellites with coarser spatial resolution, or an intensive ground campaign to develop a bottom-up inventory. The

https://doi.org/10.5194/egusphere-2026-4693
Preprint. Discussion started: 15 September 2026

information content of MethaneSAT data allowed for inversions with spatial and temporal resolution previously unfeasible with existing satellite observations. The close correspondence of the MFIM and CORE models, when averaged over a modest number of scenes, lends confidence that regional methane flux estimates from MethaneSAT are robust against differences in modeled transport. This is an important step towards the ability to comprehensively monitor and mitigate emissions using a framework based on observations with high precision and fine spatial resolution.

Code and data availability

The code used for this analysis is available on GitHub at github.com/jacobbushey/MFIM. MethaneSAT Level 3 data and CORE results are available from the MethaneSAT portal (https://portal.MethaneSAT.org/en/emissions-map) and Google Earth Engine (https://developers.google.com/earth-engine/datasets/publisher/edf-MethaneSAT-ee), excluding the data from 2024-10-13, which will be made available upon reasonable request. Emission estimates from MFIM are available on Zenodo (10.5281/zenodo.21792549).

Author contributions

Jacob B.H. Bushey constructed the modeling framework and performed the analysis. Michael Bertolacci constructed the HMC sampler. Joshua Benmergui, Marvin Knapp, Ethan Kyzivat, Sasha Ayvazov and Marcus Russi contributed to the design of the modeling framework. Julian Kostinek contributed considerably to our understanding of FLEXPART. Maryann Sargent, Ju Chulakadabba and Zhan Zhang quantified the distinct sources. Sébastien Roche and Christopher Chan Miller contributed to our understanding of how to incorporate the averaging kernel into the model. Lucas A. Estrada shared data from his inversion and gave helpful feedback on the manuscript. James D. East shared data from his inversion and gave important insights into the uncertainty bounds in his paper. Luna Yin contributed to the development of the box model. James P. Williams, Anthony Himmelberger and Ritesh Gautam created the Permian inversion composite and compared these results to other studies of the Permian. Mark Omara provided insights into the EI-ME. Steven C. Wofsy and Jia Chen provided insight and edited the paper. Jacob B.H. Bushey wrote the paper with input from all authors.

Competing interests

The authors declare no competing interests

Acknowledgements

We gratefully acknowledge all members of the MethaneAIR and MethaneSAT teams who contributed to the mission, instrument calibration, and data collection and analysis. Thanks to Petra Seibert, Marinä Dutsch, Rona Thompson and Lokahith Narendra Agasthya for their help troubleshooting the FLEXPART model setup. Special thanks to Ethan Manninen for helpful

https://doi.org/10.5194/egusphere-2026-4693
Preprint. Discussion started: 15 September 2026

discussions of model transport uncertainties and the differences between quantifying distinct and dispersed sources. Thanks to Daniel Varon for a helpful explanation of his results.

Financial support

This research has been supported by the National Science Foundation grant (AGS-2202113 and EAGER grant 1856426) as well as the Environmental Defense Fund. For a more complete list of funders, please visit https://www.MethaneSAT.org/ (last access: 12 December 2025). TUM authors were partially funded by the EU projects "PAUL" (Grant 101037319) and "CoSense4Climate" (Grant 101089203).

https://doi.org/10.5194/egusphere-2026-4693
Preprint. Discussion started: 15 September 2026

Appendix A: Model and MCMC Sampler

With the choices detailed above, the truncated multivariate Gaussian prior for $\boldsymbol{x}$ has density

$$p(\boldsymbol{x} \mid \sigma_0^2) \propto \sigma_0^{-n} \exp\left(-\frac{1}{2\sigma_0^2}\boldsymbol{x}^T\boldsymbol{x}\right) 1(\boldsymbol{x} > \mathbf{0}), \tag{A1}$$

where the proportionality sign indicates that the constant of proportionality does not depend on $\boldsymbol{x}$ or σ_0^2, and $1(\boldsymbol{x} > \mathbf{0})$ is an indicator that evaluates to 1 if all elements of $\boldsymbol{x}$ are positive, and zero otherwise. The multivariate (not truncated) Gaussian prior on the error vector $\boldsymbol{e}$ has density

$$p(\boldsymbol{e} \mid \sigma_e^2) \propto \sigma_e^{-m} \exp\left(-\frac{1}{2\sigma_e^2}\boldsymbol{e}^T\mathbf{C}_e^{-1}\boldsymbol{e}\right). \tag{A2}$$

Here, $\mathbf{C}_e$ is an $m \times m$ correlation matrix with diagonal entries equal to one, and (i,j)th off-diagonal entry equal to $\exp(-d_{ij}/l_e)$, where d_{ij} is the distance in kilometers between observations i and j, and l_e is the error correlation e-folding length, set equal to 1 km. Since $\boldsymbol{y} = \mathbf{K}\boldsymbol{x} + \boldsymbol{e}$, the above implies that

$$p(\boldsymbol{y} \mid \boldsymbol{x}, \sigma_e^2) \propto \sigma_e^{-m} \exp\left(-\frac{1}{2\sigma_e^2}(\boldsymbol{y} - \mathbf{K}\boldsymbol{x})^T\mathbf{C}_e^{-1}(\boldsymbol{y} - \mathbf{K}\boldsymbol{x})\right). \tag{A3}$$

The parameters σ_0^2 and σ_e^2 are unknown are hence the priors on $\boldsymbol{x}$ and $\boldsymbol{e}$ are unknown. As is common practice, we assign inverse gamma prior distributions to both variance parameters, so that their densities are, respectively,

$$p(\sigma_0^2) \propto (\sigma_0^2)^{a_0-1} e^{-\frac{b_0}{\sigma_0^2}},\ p(\sigma_e^2) \propto (\sigma_e^2)^{a_e-1} e^{-\frac{b_e}{\sigma_e^2}}. \tag{A4}$$

We let a = b = 0, which corresponds to a highly non-informative prior on σ_0^2 and σ_e^2.

Inference using MCMC

The full posterior distribution over the unknowns is given by

$$p(\boldsymbol{x}, \sigma_0^2, \sigma_e^2 \mid \boldsymbol{y}) \propto p(\boldsymbol{y} \mid \boldsymbol{x}, \sigma_e^2)\, p(\boldsymbol{x} \mid \sigma_0^2)\, p(\sigma_e^2) p(\sigma_0^2), \tag{A5}$$

but the distribution of most interest is the marginal posterior distribution over the flux state vector, which is given by

$$p(\boldsymbol{x} \mid \boldsymbol{y}) = \iint p(\boldsymbol{x}, \sigma_0^2, \sigma_e^2 \mid \boldsymbol{y})\, d\sigma_0^2\, d\sigma_e^2. \tag{A6}$$

This integral is intractable in general, and due to the truncated Gaussian prior and the unknown variance parameters, it doesn't correspond to a closed-form distribution such as a multivariate Gaussian. Instead, we use MCMC to generate joint samples $\left(\boldsymbol{x}^{[s]}, (\sigma_0^2)^{[s]}, (\sigma_e^2)^{[s]}\right)$, $s = 1, \dots, S$,

https://doi.org/10.5194/egusphere-2026-4693
Preprint. Discussion started: 15 September 2026

from the full posterior $p(\boldsymbol{x}, \sigma_0^2, \sigma_e^2 \mid \boldsymbol{y})$; then the samples $\boldsymbol{x}^{[s]}$ can be taken to be a sample from $p(\boldsymbol{x} \mid \boldsymbol{y})$.

The MCMC sampler we use is a Gibbs sampler that works as follows: starting from an initial value $\left(\boldsymbol{x}^{[1]}, \left(\sigma_0^2\right)^{[1]}, (\sigma_e^2)^{[1]}\right)$, for sample indices $s = 2, \dots, S$,

1. Sample $\boldsymbol{x}^{[s]}$ from $p(\boldsymbol{x} \mid \boldsymbol{y}, (\sigma_0^2)^{[s-1]}, (\sigma_e^2)^{[s-1]})$;
2. Sample $(\sigma_0^2)^{[s]}$ from $p(\sigma_0^2 \mid \boldsymbol{x}^{[s]})$;
3. Sample $(\sigma_e^2)^{[s]}$ from $p(\sigma_e^2 \mid \boldsymbol{y}, \boldsymbol{x}^{[s]})$.

Usually, the first few hundred samples from this procedure are discarded as "burn-in", which is the time the sampler needs to reach a region of high density. Then the remaining samples constitute a joint sample from the full posterior distribution. The key to the Gibbs sampler is that each individual step is easier than sampling from the joint distribution itself due to the simpler nature of the conditional distributions. The next section gives each of these conditionals in turn and describe how to sample from them.

Conditional distributions

The conditional distribution $p(\boldsymbol{x} \mid \boldsymbol{y}, \sigma_0^2, \sigma_e^2)$ can be shown to equal a truncated multivariate Gaussian distribution $N_+(\hat{\boldsymbol{x}}, \hat{\mathbf{S}})$, where

$$\hat{\mathbf{S}} = (\sigma_e^{-2}\mathbf{K}^T\mathbf{C}_e^{-1}\mathbf{K} + \sigma_0^{-2}\boldsymbol{I}_n)^{-1} \quad \text{and} \quad \hat{\boldsymbol{x}} = \sigma_e^{-2}\mathbf{S}\mathbf{K}^T\mathbf{C}_e^{-1}\boldsymbol{y}. \tag{A7}$$

This distribution has the same mean and covariance matrix as when the prior is an *untruncated* multivariate Gaussian prior, which is the most common choice in flux inversion; the only difference is the truncation. As a result, its density is

$$p(\boldsymbol{x} \mid \boldsymbol{y}, \sigma_0^2, \sigma_e^2) \propto \left|\hat{\mathbf{S}}\right|^{-\frac{1}{2}} \exp\left(-\tfrac{1}{2}(\boldsymbol{x} - \hat{\boldsymbol{x}})^T\, \hat{\mathbf{S}}^{-1}(\boldsymbol{x} - \hat{\boldsymbol{x}})\right) 1(\boldsymbol{x} > \mathbf{0}). \tag{A8}$$

Exact inference for this distribution is difficult, but algorithms exist for efficiently drawing samples from it. In particular, Pakman and Paninski (2014) present an efficient HMC algorithm for sampling from this distribution; this uses exact Hamiltonian dynamics simulation to propose new states. We use this algorithm in our implementation of the Gibbs sampler.

The conditional distributions $p(\sigma_0^2 \mid \boldsymbol{x})$ and $p(\sigma_e^2 \mid \boldsymbol{y}, \boldsymbol{x})$ are both inverse gamma distributions, the same family as their prior. They are given by

$$p(\sigma_0^2 \mid \boldsymbol{x}) \propto (\sigma_0^2)^{\hat{a}_0 - 1} e^{-\frac{\hat{b}_0}{\sigma_0^2}}, \;\; p(\sigma_e^2 \mid \boldsymbol{y}, \boldsymbol{x}) \propto (\sigma_e^2)^{\hat{a}_e - 1} e^{-\frac{\hat{b}_e}{\sigma_e^2}}, \tag{A9}$$

https://doi.org/10.5194/egusphere-2026-4693
Preprint. Discussion started: 15 September 2026

where

$$\hat{a}_0 = a_0 + \frac{n}{2}, \qquad \hat{b}_0 = b_0 + \frac{1}{2}\boldsymbol{x}^T\boldsymbol{x}$$
$$\hat{a}_e = a_e + \frac{m}{2}, \quad \hat{b}_e = b_e + \frac{1}{2}(\boldsymbol{y} - \mathbf{K}\boldsymbol{x})^T\mathbf{C}_e^{-1}(\boldsymbol{y} - \mathbf{K}\boldsymbol{x}). \tag{A10}$$

Sampling from these distributions is standard and can be done using existing software routines.

https://doi.org/10.5194/egusphere-2026-4693
Preprint. Discussion started: 15 September 2026

Appendix B: Averaging Kernel Treatment

While there is a different averaging kernel for each pixel, based on viewing geometry, aerosol vertical profile, temperature profile, surface albedo and other factors, we chose to use a single representative averaging kernel for every simulated observation from FLEXPART. This approach assumes that if MethaneSAT were to make observations of our FLEXPART output it would do so above a uniform surface, through a uniform atmosphere and from a uniform viewing geometry, and follows the example of Hungershoefer et al. (2010). Because the dominant difference between averaging kernels is a scaling factor, which would average out spatially across the domain, this assumption is acceptable for our purposes, which is to capture the greater sensitivity of the column-averaged dry-air mole fraction to methane enhancements in the lower atmosphere. We compared the average and interquartile range of the averaging kernels across each scene and found that this is an acceptable assumption that will not impact our final emission estimates. This does not necessarily mean that the averaging kernel is physically correct, as Buchwitz et al. (2006) have shown that they can cause enhancements to be over or underestimates, but rather that the model needs to be adjusted in order to be comparable to the observations.

Eq. B1 is used to convert from mixing ratios at each layer to column-averaged dry-air mole fraction.

$$XCH_4 \approx \sum_{i=1}^{55}\left(\frac{dp_i}{p_{surf}} * a_i * n_i\right), \tag{B1}$$

Where a_i is the averaging kernel weighting function at each level, $\frac{dp_i}{p_{surf}}$ is the column weighting function (pressure difference across that layer normalized so that all layers add to 1) and n_i is the mole fraction of CH_4 for each layer. The averaging kernel is interpolated onto 55 vertical layers throughout the simulated atmospheric column. We are able to approximate by using mixing ratio instead of vertical column density (VCD) because of uniform grid box pressure differences in the lower atmosphere, where the methane enhancement in our model is found. This requires the assumption that there is no bias in the TCCON CO_2 product used in the retrieval, that the prior is an accurate regional background and has no bias, and that we can neglect the influence of water vapor (which is negligible in a dry region like the Permian Basin). These assumptions also allow

https://doi.org/10.5194/egusphere-2026-4693
Preprint. Discussion started: 15 September 2026

us to neglect the impact that the CO_2 averaging kernel would have through the use of the proxy retrieval algorithm.

In order to apply the MethaneSAT averaging kernel to the modeled atmosphere in FLEXPART, we weight the particle releases at each layer by a_i and $\frac{dp_i}{p_{surf}}$ (which can be neglected because the particles are released from layers of approximately equal pressure thickness).

Previous studies have shown that excluding the averaging kernel from the analysis has a negligible impact on the results, especially considered relative to transport errors and instrument noise (Li et al., 2022; Connor et al., 2008; Cogan et al., 2012; Zheng et al., 2019). This further strengthens the argument for using this simplified version of the averaging kernel. Averaging kernel discrepancies arising from this assumption will average out over the entirety of a domain and will be dominated by errors in the atmospheric transport model. They will therefore have a minimal influence on the basin total emission estimate.

https://doi.org/10.5194/egusphere-2026-4693
Preprint. Discussion started: 15 September 2026

Appendix C: Relative contribution of source types

The total emissions of an oil and gas basin may be considered to represent the sum of distinct sources and dispersed sources. Distinct sources are identifiable as discrete plumes or blobs. Diffuse sources are more diffuse across space, representing cumulative emissions from distributed sources not identifiable as distinct sources. The distinction between these two types of sources depends on the sensitivity and detection limit of the observing platform, wind conditions at the time of observations, and other factors (Manninen et al., 2026). Under ideal viewing conditions, a distinct source detectable by MethaneSAT is any source emitting above the distinct source detection threshold of ~1300 kg/hr (Guanter et al., 2026; Manninen et al., 2026). The relative contribution of distinct and dispersed sources to basin total emissions (i.e. the statistical distribution of the emission magnitudes) is a current topic of discussion in the literature (Omara et al., 2024; Sherwin et al., 2024), and depends on the detection threshold of the observing system. MethaneSAT quantifies emissions from both source types simultaneously, spanning the gap between area flux mappers (Jacob et al., 2022) like TROPOMI (Tropospheric Monitoring Instrument, Veefkind et al. 2023, 5 km x 7 km pixel size) and point source imagers like GHGSat (Jervis et al., 2021, 25 x 25 m^2 nadir pixels) and Carbon Mapper's Tanager-1 (Duren et al., 2025, 30 x 30 m^2).

Comparing the basin totals to the quantified distinct sources in each data set allows us to calculate the relative contribution of distinct sources to the basin total. Taking the sum of all distinct sources and the sum of all dispersed sources, we find that the distinct sources contribute only 6.0% of total emissions across all 9 scenes. This supports the conclusions of Williams et al. (2025) that dispersed sources make up the majority of emissions from oil and gas basins within the continental United States.

https://doi.org/10.5194/egusphere-2026-4693
Preprint. Discussion started: 15 September 2026

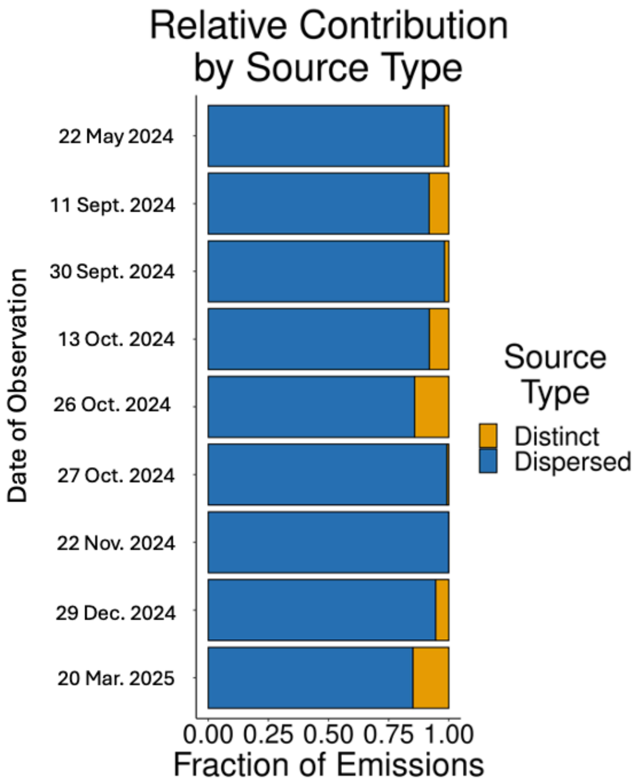

875

Figure C1. The relative contribution of distinct sources to basin total emissions for the domains. This data suggests that dispersed sources make up the majority of emissions in the Permian Basin.

880

https://doi.org/10.5194/egusphere-2026-4693
Preprint. Discussion started: 15 September 2026

Appendix D: Adjusting the MFIM background to match CORE

We use a version of MFIM where the background has been adjusted such that the mean of the observed enhancement equals the mean of the posterior modeled enhancement from CORE (listed as MFIM_adj in Fig. 6) to assess the sensitivity of model results to the background concentration assumptions. When averaging across individual scenes, MFIM_adj is higher than CORE by an average of 15.1%. We conclude that the models agree well when averaging across many individual scenes, regardless of whether the adjusted background is used.

When compiling the individual scenes into a composite emissions estimate, MFIM_adj has a basin total of 488 tons/hr, which is higher than the MFIM base case results by 22.6%, further demonstrating the importance of the background estimation for controlling the basin total. The MFIM_adj basin total is larger than CORE by 33.3%, near the level of agreement documented by other studies using different transport models (Munassar et al., 2023) and just outside of the uncertainty estimate (95% CI 282-453 tons/hr), although the CORE results fall within the uncertainty estimate for MFIM_adj (288-688 tons/hr). This discrepancy is likely due to the regularizing effect of the prior on emissions from CORE. The optimization of the background offset in CORE tends to push the background concentration down, which would increase the average enhancement. This would lead to a widespread increase in emissions if not for the prior, which prevents the model from fitting noise in low emitting regions. Since MFIM_adj uses a spatially invariant prior, this compensatory effect is not present, so lowering the background to match the average enhancement from CORE only increases emissions. Therefore it is more appropriate to compare CORE to the MFIM base case.

https://doi.org/10.5194/egusphere-2026-4693
Preprint. Discussion started: 15 September 2026

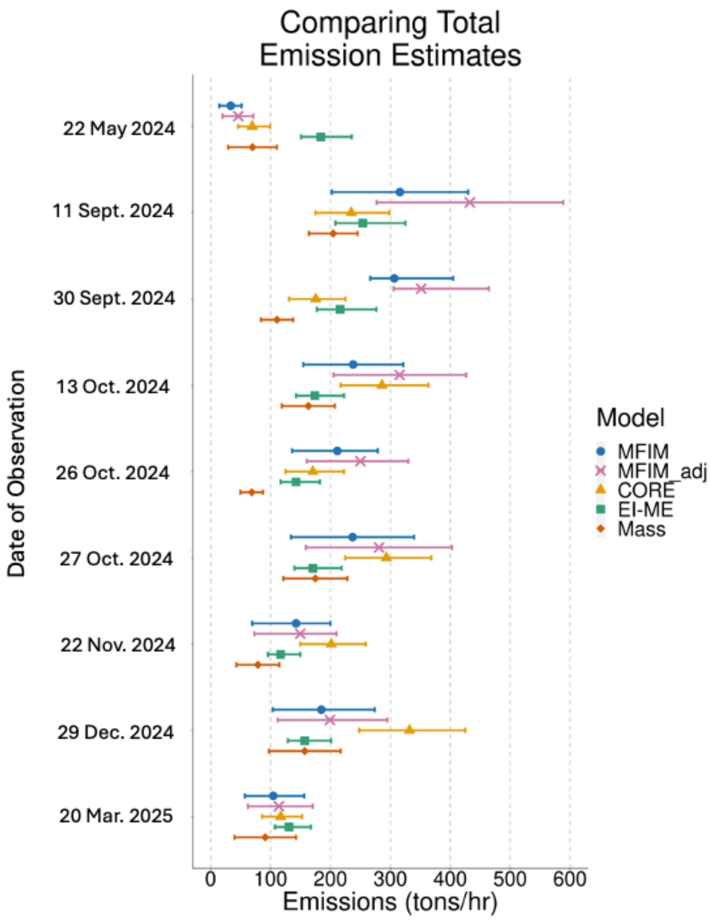

Figure D1. The same data presented in Fig. 6, now including the MFIM_adj case. Error bars for
905 MFIM with the CORE background scale the uncertainty from CORE to the new total emission estimate.

https://doi.org/10.5194/egusphere-2026-4693
Preprint. Discussion started: 15 September 2026

References

Allen, D. T.: Methane emissions from natural gas production and use: Reconciling bottom-up and top-down measurements. Current Opinion in Chemical Engineering, 5, 78–83. https://doi.org/10.1016/j.coche.2014.05.004, 2014.

Bakels, L., Tatsii, D., Tipka, A., Thompson, R., Dütsch, M., Blaschek, M., Seibert, P., Baier, K., Bucci, S., Cassiani, M., Eckhardt, S., Groot Zwaaftink, C., Henne, S., Kaufmann, P., Lechner, V., Maurer, C., Mulder, M. D., Pisso, I., Plach, A., Subramanian, R., Vojta, M., Stohl, A.: FLEXPART version 11: Improved accuracy, efficiency, and flexibility. Geosci. Model Dev., 17(21), 7595–7627. https://doi.org/10.5194/gmd-17-7595-2024, 2024

Basu, S., Baker, D. F., Chevallier, F., Patra, P. K., Liu, J., and Miller, J. B.: The impact of transport model differences on CO_2 surface flux estimates from OCO-2 retrievals of column average CO_2. Atmos. Chem. Phys., 18(10), 7189–7215. https://doi.org/10.5194/acp-18-7189-2018, 2018.

Brasseur, G. P., and Jacob, D. J., Modeling of Atmospheric Chemistry, Cambridge University Press, 2017.

Bertolacci, M., Zammit-Mangion, A., Schuh, A., Bukosa, B., Fisher, J., Cao, Y., Kaushik, A., and Cressie, N.: Inferring changes to the global carbon cycle with WOMBAT v2.0, a hierarchical flux-inversion framework. arXiv. https://doi.org/10.48550/arXiv.2210.10479, 2022

Buchwitz, M., De Beek, R., Noël, S., Burrows, J. P., Bovensmann, H., Schneising, O., Khlystova, I., Bruns, M., Bremer, H., Bergamaschi, P., Körner, S., and Heimann, M.: Atmospheric carbon gases retrieved from SCIAMACHY by WFM-DOAS: version 0.5 CO and CH_4 and impact of calibration improvements on CO_2 retrieval, Atmospheric Chemistry and Physics, 6, 2727–2751, https://doi.org/10.5194/acp-6-2727-2006, 2006.

Butz, A., Hasekamp, O. P., Frankenberg, C., Vidot, J., and Aben, I.: CH_4 retrievals from space-based solar backscatter measurements: Performance evaluation against simulated aerosol and cirrus loaded domains, J. Geophys. Res.-Atmos., 115, 2010JD014 514, https://doi.org/10.1029/2010JD014514, 2010.

Carpenter, B., Gelman, A., Hoffman, M. D., Lee, D., Goodrich, B., Betancourt, M., Brubaker, M., Guo, J., Li, P., and Riddell, A.: Stan: A Probabilistic Programming Language. J. Stat. Softw., 76(1). https://doi.org/10.18637/jss.v076.i01, 2017.

Chan Miller, C., Roche, S., Wilzewski, J. S., Liu, X., Chance, K., Souri, A. H., Conway, E., Luo, B., Samra, J., Hawthorne, J., Sun, K., Staebell, C., Chulakadabba, A., Sargent, M., Benmergui, J. S., Franklin, J. E., Daube, B. C., Li, Y., Laughner, J. L., Baier, B. C., Gautam, R., Omara, M., and Wofsy, S. C.: Methane retrieval from MethaneAIR using the CO_2 proxy approach: a demonstration for the upcoming MethaneSAT mission, Atmos. Meas. Tech., 17, 5429–5454, https://doi.org/10.5194/amt-17-5429-2024, 2024.

Chan Miller, C., Roche, S., Wilzweski, J., Liu, X., Chance, K. V., Luo, B., Sun, K., Franklin, J. E., Benmergui, J. S., Nasr, M., Miller, D. J., Crowell, S., Leisso, N., Walker, E., Gautam, R., LoFaso, N., Ayvazov, S., Wells, D., Cervantes, C., Hairfield, C., and Wofsy, S.: Operational XCH_4 Retrievals from MethaneSAT: Demonstrating Sensor Performance for Constraining Regional Methane Emissions, EGUsphere [preprint], https://doi.org/10.5194/egusphere-2026-3365, 2026.

Chulakadabba, A., Sargent, M., Lauvaux, T., Benmergui, J. S., Franklin, J. E., Chan Miller, C., Wilzewski, J. S., Roche, S., Conway, E., Souri, A. H., Sun, K., Luo, B., Hawthrone, J., Samra, J., Daube, B. C., Liu, X., Chance, K., Li, Y., Gautam, R., Omara, M., Rutherford, J. S., Sherwin, E. D., Brandt, A., and Wofsy, S. C.: Methane point source quantification using MethaneAIR: a new airborne imaging spectrometer, Atmos. Meas. Tech., 16, 5771–5785, https://doi.org/10.5194/amt-16-5771-2023, 2023.

Cogan, A. J., Boesch, H., Parker, R. J., Feng, L., Palmer, P. I., Blavier, J. L., Deutscher, N. M., Macatangay, R., Notholt, J., Roehl, C., Warneke, T., and Wunch, D.: Atmospheric carbon dioxide retrieved from the Greenhouse gases Observing SATellite (GOSAT): Compari- son with ground-based TCCON observations and GEOS-Chem model calculations, J. Geophys. Res.-Atmos., 117, 2012JD018 087, https://doi.org/10.1029/2012JD018087, 2012.

Connor, B. J., Boesch, H., Toon, G., Sen, B., Miller, C., and Crisp, D.: Orbiting Carbon Observatory: Inverse method and prospective error analysis, J. Geophys. Res.-Atmos., 113, 2006JD008 336, https://doi.org/10.1029/2006JD008336, 2008.

Deng, A., Lauvaux, T., Davis, K. J., Gaudet, B. J., Miles, N., Richardson, S. J., Wu, K., Sarmiento, D. P., Hardesty, R. M., Bonin, T. A., Brewer, W. A., and Gurney, K. R.: Toward reduced transport errors in a high resolution urban CO2 inversion system, Elementa: Elem. Sci. Anthropocene, 5, 20, https://doi.org/10.1525/elementa.133, 2017.

https://doi.org/10.5194/egusphere-2026-4693
Preprint. Discussion started: 15 September 2026

Deng, F., Jones, D. B. A., Henze, D. K., Bousserez, N., Bowman, K. W., Fisher, J. B., Nassar, R., O'Dell, C., Wunch, D., Wennberg, P. O., Kort, E. A., Wofsy, S. C., Blumenstock, T., Deutscher, N. M., Griffith, D. W. T., Hase, F., Heikkinen, P., Sherlock, V., Strong, K., Sussmann, R., and Warneke, T.: Inferring regional sources and sinks of atmospheric CO_2 from GOSAT XCO_2 data, Atmos. Chem. Phys., 14, 3703–3727, https://doi.org/10.5194/acp-14-3703-2014, 2014.

Duren, R., Cusworth, D., Ayasse, A., Howell, K., Diamond, A., Scarpelli, T., Kim, J., O'neill, K., Lai-Norling, J., Thorpe, A., Zandbergen, S. R., Shaw, L., Keremedjiev, M., Guido, J., Giuliano, P., Goldstein, M., Nallapu, R., Barentsen, G., Thompson, D. R., Roth, K., Jensen, D., Eastwood, M., Reuland, F., Adams, T., Brandt, A., Kort, E.A., Mason, J., and Green, R. O.: The Carbon Mapper emissions monitoring system. Atmos. Meas. Tech., 18(22), 6933–6958. https://doi.org/10.5194/amt-18-6933-2025, 2025.

East, J. D., Jacob, D. J., Jervis, D., Balasus, N., Estrada, L. A., Hancock, S. E., Sulprizio, M. P., Thomas, J., Wang, X., Chen, Z., Varon, D. J., and Worden, J. R.: Worldwide inference of national methane emissions by inversion of satellite observations with UNFCCC prior estimates. Nat. Commun., 16(1), 11004. https://doi.org/10.1038/s41467-025-67122-8, 2025.

Eckhardt, S., Prata, A. J., Seibert, P., Stebel, K., and Stohl, A.: Estimation of the vertical profile of sulfur dioxide injection into the atmosphere by a volcanic eruption using satellite column measurements and inverse transport modeling, Atmos. Chem. Phys., https://doi.org/10.5194/acp-8-3881-2008, 2008.

Estrada, L. A., Jacob, D. J., He, M., East, J. D., Varon, D. J., Balasus, N., Hancock, S. E., Sulprizio, M., Bowman, K. W., Worden, J. R., Reidy, E., and Runkle, B. R. K.: Quantifying national, state, and oil/gas field methane emissions and trends in the US (2019–2024) through high resolution inversion of satellite observations, Atmos. Chem. Phys., 26, 10629–10646, https://doi.org/10.5194/acp-26-10629-2026, 2026.

Ganesan, A. L., Rigby, M., Zammit-Mangion, A., Manning, A. J., Prinn, R. G., Fraser, P. J., Harth, C. M., Kim, K.-R., Krummel, P. B., Li, S., Mühle, J., O'Doherty, S. J., Park, S., Salameh, P. K., Steele, L. P., and Weiss, R. F.: Characterization of uncertainties in atmospheric trace gas inversions using hierarchical Bayesian methods. Atmos. Chem. Phys., 14(8), 3855–3864. https://doi.org/10.5194/acp-14-3855-2014, 2014.

Gaudet, L. C., Sulia, K. J., Torn, R. D., and Bassill, N. P.: Verification of the Global Forecast System, North American Mesoscale Forecast System, and High-Resolution Rapid Refresh Model Near-Surface Forecasts by use of the New York State Mesonet. Wea. Forecasting, 39(2), 369–386. https://doi.org/10.1175/WAF-D-23-0094.1, 2024.

Guanter, L., Roger, J., Warren, J., Sargent, M., Zhang, Z., Roche, S., Miller, C. C., Steiner, M., Hadfield, H., Omara, M., Williams, J., MacKay, K., Franklin, J. E., Luo, B., Wofsy, S. C., Hamburg, S. P., and Gautam, R.: Surveying methane point-source super-emissions across oil and gas basins with MethaneSAT, Atmos. Chem. Phys., 26, 2941–2963, https://doi.org/10.5194/acp-26-2941-2026, 2026.

He, C., Lu, X., Zhang, Y., Liu, Z., Jiang, F., Sun, Y., Gao, M., Liu, Y., Lin, H., Yang, J., Lin, X., Wang, Y., Hu, C., and Fan, S.: Revisiting the quantification of power plant CO2 emissions in the United States and China from satellite: A comparative study using three top-down approaches, Remote. Sens. Environ., 308, 114 192, https://doi.org/10.1016/j.rse.2024.114192, 2024.

Houweling, S., Aben, I., Breon, F.-M., Chevallier, F., Deutscher, N., Engelen, R., Gerbig, C., Griffith, D., Hungershoefer, K., Macatan- gay, R., Marshall, J., Notholt, J., Peters, W., and Serrar, S.: The importance of transport model uncertainties for the estimation of CO_2 sources and sinks using satellite measurements, Atmos. Chem. Phys., 10, 9981–9992, https://doi.org/10.5194/acp-10-9981-2010, 2010.

Hungershoefer, K., Breon, F.-M., Peylin, P., Chevallier, F., Rayner, P., Klonecki, A., Houweling, S., and Marshall, J.: Evaluation of various observing systems for the global monitoring of CO_2 surface fluxes, Atmos. Chem. Phys., 10, 10 503–10 520, https://doi.org/10.5194/acp-10-10503-2010, 2010.

Jacob, D. J., Varon, D. J., Cusworth, D. H., Dennison, P. E., Frankenberg, C., Gautam, R., Guanter, L., Kelley, J., McKeever, J., Ott, L. E., Poulter, B., Qu, Z., Thorpe, A. K., Worden, J. R., and Duren, R. M.: Quantifying methane emissions from the global scale down to point sources using satellite observations of atmospheric methane, Atmos. Chem. Phys., 22, 9617–9646, https://doi.org/10.5194/acp-22-9617-2022, 2022.

Jervis, D., McKeever, J., Durak, B. O. A., Sloan, J. J., Gains, D., Varon, D. J., Ramier, A., Strupler, M., and Tarrant, E.: The GHGSat-D imaging spectrometer. Atmos. Meas. Tech., 14(3), 2127–2140. https://doi.org/10.5194/amt-14-2127-2021, 2021.

https://doi.org/10.5194/egusphere-2026-4693
Preprint. Discussion started: 15 September 2026

Laughner, J. L., Roche, S., Kiel, M., Toon, G. C., Wunch, D., Baier, B. C., Biraud, S., Chen, H., Kivi, R., Laemmel, T., McKain, K., Quéhé, P.-Y., Rousogenous, C., Stephens, B. B., Walker, K., and Wennberg, P. O.: A new algorithm to generate a priori trace gas profiles for the GGG2020 retrieval algorithm, Atmos. Meas. Tech., 16, 1121–1146, https://doi.org/10.5194/amt-16-1121-2023, 2023.

Laughner, J. L., Toon, G. C., Mendonca, J., Petri, C., Roche, S., Wunch, D., Blavier, J.-F., Griffith, D. W. T., Heikkinen, P., Keeling, R. F., Kiel, M., Kivi, R., Roehl, C. M., Stephens, B. B., Baier, B. C., Chen, H., Choi, Y., Deutscher, N. M., DiGangi, J. P., Gross, J., Herkommer, B., Jeseck, P., Laemmel, T., Lan, X., McGee, E., McKain, K., Miller, J., Morino, I., Notholt, J., Ohyama, H., Pollard, D.F., Rettinger, M., Riris, H., Rousogenous, C., Kumar Sha, M., Shiomi, K., Strong, K., Sussmann, R., Té, Y., Velazco, V.A., Wofsy, S.C., Zhyou, M., and Wennberg, P. O.: The Total Carbon Column Observing Network's GGG2020 data version. Earth Sys. Sci. Data, 16(5), 2197–2260. https://doi.org/10.5194/essd-16-2197-2024, 2024.

Lauvaux, T. and Davis, K. J.: Planetary boundary layer errors in mesoscale inversions of column-integrated CO_2 measurements, J. Geophys. Res.-Atmos., 119, 490–508, https://doi.org/10.1002/2013JD020175, 2014.

Li, L., Lei, L., Song, H., Zeng, Z., and He, Z.: Spatiotemporal Geostatistical Analysis and Global Mapping of CH4 Columns from GOSAT Observations, Remote Sensing, 14, 654, https://doi.org/10.3390/rs14030654, 2022.

Lin, J. C., Gerbig, C., Wofsy, S. C., Andrews, A. E., Daube, B. C., Davis, K. J., and Grainger, C. A.: A near-field tool for simulating the up- stream influence of atmospheric observations: The Stochastic Time-Inverted Lagrangian Transport (STILT) model, J. Geophys. Res.-Atmos., 108, https://doi.org/10.1029/2002jd003161, 2003.

Lin, X., Van Der A, R., De Laat, J., Eskes, H., Chevallier, F., Ciais, P., Deng, Z., Geng, Y., Song, X., Ni, X., Huo, D., Dou, X., and Liu, Z.: Monitoring and quantifying CO_2 emissions of isolated power plants from space. Atmos. Chem. Phys., 23(11), 6599–6611. https://doi.org/10.5194/acp-23-6599-2023, 2023

Liu, M., van der A, R., van Weele, M., Eskes, H., Lu, X., Veefkind, P., de Laat, J., Kong, H., Wang, J., Sun, J., Ding, J., Zhao, Y., and Weng, H.: A New Divergence Method to Quantify Methane Emissions Using Observations of Sentinel-5P TROPOMI. Geophys. Res. Lett., 48(18), e2021GL094151. https://doi.org/10.1029/2021GL094151, 2021.

https://doi.org/10.5194/egusphere-2026-4693
Preprint. Discussion started: 15 September 2026

Locatelli, R., Bousquet, P., Chevallier, F., Fortems-Cheney, A., Szopa, S., Saunois, M., Agusti-Panareda, A., Bergmann, D., Bian, H., Cameron-Smith, P., Chipperfield, M. P., Gloor, E., Houweling, S., Kawa, S. R., Krol, M., Patra, P. K., Prinn, R. G., Rigby, M., Saito, R., and Wilson, C.: Impact of transport model errors on the global and regional methane emissions estimated by inverse modelling, Atmos. Chem. Phys., 13, 9917–9937, https://doi.org/10.5194/acp-13-9917-2013, 2013.

MacKay, K., Benmergui, J., Williams, J. P., Omara, M., Himmelberger, A., Sargent, M., Warren, J. D., Miller, C. C., Roche, S., Zhang, Z., Franklin, J., Guanter, L., Wofsy, S., and Gautam, R.: Assessment of methane emissions from US onshore oil and gas production using MethaneAIR measurements. Atmos. Chem. Phys., 26(2), 1179–1192. https://doi.org/10.5194/acp-26-1179-2026, 2026.

Maasakkers, J. D., McDuffie, E. E., Sulprizio, M. P., Chen, C., Schultz, M., Brunelle, L., Thrush, R., Steller, J., Sherry, C., Jacob, D. J., Jeong, S., Irving, B., and Weitz, M.: A Gridded Inventory of Annual 2012–2018 U.S. Anthropogenic Methane Emissions. Environ. Sci. Technol., 57(43), 16276–16288. https://doi.org/10.1021/acs.est.3c05138, 2023.

Maier, F., Koch, F.-T., Munassar, S., Rödenbeck, C., and Gerbig, C. et al. (2025): How reliable are process-based ^{222}Rn emission maps? Results from an atmospheric ^{222}Rn inversion in Europe. *Atmospheric Chemistry and Physics*, https://doi.org/10.5194/acp-25-12779-2025, 2025.

Manninen, E., Chulakadabba, A., Sargent, M., Zhang, Z., Kamdar, H., Warren, J., Roche, S., Chan Miller, C., Kyzivat, E., Benmergui, J., Pittman, J., Walker, E., Bushey, J., Samra, J., Hawthorne, J., Luo, B., Nasr, M., Sun, K., Franklin, J., Liu, X., Chen, J., and Wofsy, S.: Probabilities of Detection of Methane Plumes by Remote Sensing and Implications for Inferred Emissions Distributions, EGUsphere [preprint], https://doi.org/10.5194/egusphere-2026-115, 2026.

McDuffie, E. E., Maasakkers, J. D., Sulprizio, M. P., Chen, C., Schultz, M., Brunelle, L., Thrush, R., Steller, J., Sherry, C., Jacob, Daniel, J., Jeong, S., Irving, B., and Weitz, M.: Gridded EPA U.S. Anthropogenic Methane Greenhouse Gas Inventory (gridded GHGI) (v1.0) [Data set]. Zenodo. https://doi.org/10.5281/zenodo.8367082, 2023.

Mengistu, A. G., Tsuruta, A., Berchet, A., Thompson, R., Tenkanen, M., Lindqvist, H., Markkanen, T., Leppänen, A., Laitinen, A., Martinez, A., Fortems-Cheiney, A., Höglund-Isaksson, L., and Aalto, T.: High-resolution inversion of methane emissions over Europe using

https://doi.org/10.5194/egusphere-2026-4693
Preprint. Discussion started: 15 September 2026

the Community Inversion Framework and FLEXPART, EGUsphere [preprint], https://doi.org/10.5194/egusphere-2025-5877, 2026.

MethaneSAT Science and Engineering Team, 2026. MethaneSAT Level-4 Dispersed Emissions Product: Algorithm Theoretical Basis Document v1.1. https://doi.org/10.5281/zenodo.20030295

Michalak, A. M.: A Gibbs sampler for inequality-constrained geostatistical interpolation and inverse modeling. Water Resour. Res., 44(9), 2007WR006645. https://doi.org/10.1029/2007WR006645, 2008.

Munassar, S., Monteil, G., Scholze, M., Karstens, U., Rödenbeck, C., Koch, F.-T., Totsche, K. U., and Gerbig, C.: Why do inverse models disagree? A case study with two European CO_2 inversions, Atmos. Chem. Phys., 23, 2813–2828, https://doi.org/10.5194/acp-23-2813-2023, 2023.

O'Dell, C. W., Connor, B., Bösch, H., O'Brien, D., Frankenberg, C., Castano, R., Christi, M., Eldering, D., Fisher, B., Gunson, M., McDuffie, J., Miller, C. E., Natraj, V., Oyafuso, F., Polonsky, I., Smyth, M., Taylor, T., Toon, G. C., Wennberg, P. O., and Wunch, D.: The ACOS CO_2 retrieval algorithm – Part 1: Description and validation against synthetic observations. Atmos. Meas. Tech., 5(1), 99–121. https://doi.org/10.5194/amt-5-99-2012, 2012.

Omara, M., Himmelberger, A., MacKay, K., Williams, J. P., Benmergui, J., Sargent, M., Wofsy, S. C., and Gautam, R.: Constructing a measurement-based spatially explicit inventory of US oil and gas methane emissions, https://doi.org/10.5194/essd-2024-72, 2024.

Pakman, A. and Paninski, L.: Exact Hamiltonian Monte Carlo for Truncated Multivariate Gaussians, http://arxiv.org/abs/1208.4118, arXiv:1208.4118 [stat], 2013.

Rodgers, C. D., and Connor, B. J.: Intercomparison of remote sounding instruments. J. Geophys. Res.-Atmos., 108(D3), 2002JD002299. https://doi.org/10.1029/2002JD002299, 2003.

Saunois, M., Bousquet, P., Poulter, B., Peregon, A., Ciais, P., Canadell, J. G., Dlugokencky, E. J., Etiope, G., Bastviken, D., Houweling, S., Janssens-Maenhout, G., Tubiello, F. N., Castaldi, S., Jackson, R. B., Alexe, M., Arora, V. K., Beerling, D. J., Bergamaschi, P., Blake, D. R., Brailsford, G., Brovkin, V., Bruhwiler, L., Crevoisier, C., Crill, P., Covey, K., Curry, C., Frankenberg, C., Gedney, N., Höglund-Isaksson, L., Ishizawa, M., Ito, A., Joos, F., Kim, H.-S., Kleinen, T., Krummel, P., Lamarque, J.-F., Langenfelds, R., Locatelli, R., Machida, T., Maksyutov, S., McDonald, K. C., Marshall, J., Melton, J. R., Morino, I., Naik, V., O'Doherty, S., Parmentier, F.-J. W., Patra, P. K., Peng, C., Peng, S., Peters, G. P., Pison, I., Prigent, C., Prinn,

https://doi.org/10.5194/egusphere-2026-4693
Preprint. Discussion started: 15 September 2026

R., Ramonet, M., Riley, W. J., Saito, M., Santini, M., Schroeder, R., Simpson, I. J., Spahni, R., Steele, P., Takizawa, A., Thornton, B. F., Tian, H., Tohjima, Y., Viovy, N., Voulgarakis, A., van Weele, M., van der Werf, G. R., Weiss, R., Wiedinmyer, C., Wilton, D. J., Wiltshire, A., Worthy, D., Wunch, D., Xu, X., Yoshida, Y., Zhang, B., Zhang, Z., and Zhu, Q.: The global methane budget 2000–2012, Earth Syst. Sci. Data, 8, 697–751, https://doi.org/10.5194/essd-8-697-2016, 2016.

Saunois, M., Martinez, A., Poulter, B., Zhang, Z., Raymond, P., Regnier, P., Canadell, J. G., Jackson, R. B., Patra, P. K., Bousquet, P., Ciais, P., Dlugokencky, E. J., Lan, X., Allen, G. H., Bastviken, D., Beerling, D. J., Belikov, D. A., Blake, D. R., Castaldi, S., Crippa, M., Deemer, B. R., Dennison, F., Etiope, G., Gedney, N., Höglund-Isaksson, L., Holgerson, M. A., Hopcroft, P. O., Hugelius, G., Ito, A., Jain, A. K., Janardanan, R., Johnson, M. S., Kleinen, T., Krummel, P., Lauerwald, R., Li, T., Liu, X., McDonald, K. C., Melton, J. R., Mühle, J., Müller, J., Murguia-Flores, F., Niwa, Y., Noce, S., Pan, S., Parker, R. J., Peng, C., Ramonet, M., Riley, W. J., Rocher-Ros, G., Rosentreter, J. A., Sasakawa, M., Segers, A., Smith, S. J., Stanley, E. H., Thanwerdas, J., Tian, H., Tsuruta, A., Tubiello, F. N., Weber, T. S., Van Der Werf, G., Worthy, D. E., Xi, Y., Yoshida, Y., Zhang, W., Zheng, B., Zhu, Q., Zhu, Q., and Zhuang, Q.: Global Methane Budget 2000–2020. https://doi.org/10.5194/essd-2024-115, 2025.

Scarpelli, T. R., Jacob, D. J., Maasakkers, J. D., Sulprizio, M. P., Sheng, J. X., Rose, K., Romeo, L., Worden, J. R., and Janssens-Maenhout, G.: A global gridded (0.1° × 0.1°) inventory of methane emissions from oil, gas, and coal exploitation based on national reports to the United Nations Framework Convention on Climate Change. Earth Sys. Sci. Data, 12(1), 563–575. https://doi.org/10.5194/essd-12-563-2020, 2020.

Scarpelli, T. R., Roy, E., Jacob, D. J., Sulprizio, M. P., Tate, R. D., and Cusworth, D. H.: Using new geospatial data and 2020 fossil fuel methane emissions for the Global Fuel Exploitation Inventory (GFEI) v3. https://doi.org/10.5194/essd-2024-552, 2025.

Schneising, O., Buchwitz, M., Reuter, M., Heymann, J., Bovensmann, H., and Burrows, J. P.: Long-term analysis of carbon dioxide and methane column-averaged mole fractions retrieved from SCIAMACHY, Atmos. Chem. Phys., 11, 2863–2880, https://doi.org/10.5194/acp-11-2863-2011, 2011.

Schneising, O., Buchwitz, M., Reuter, M., Vanselow, S., Bovensmann, H., and P. Burrows, J.: Remote sensing of methane leakage from natural gas and petroleum systems revisited, Atmos.

https://doi.org/10.5194/egusphere-2026-4693
Preprint. Discussion started: 15 September 2026

Chem. Phys., 20, 9169–9182, https://doi.org/10.5194/acp-20-9169-2020, publisher: Copernicus GmbH, 2020.

Schuh, A. E., Jacobson, A. R., Basu, S., Weir, B., Baker, D., Bowman, K., Chevallier, F., Crowell, S., Davis, K. J., Deng, F., Denning, S., Feng, L., Jones, D., Liu, J., and Palmer, P. I.: Quantifying the Impact of Atmospheric Transport Uncertainty on CO_2 Surface Flux Estimates, Global Biogeochem. Cycles, 33, 484–500, https://doi.org/10.1029/2018GB006086, 2019.

Shen, L., Zavala-Araiza, D., Gautam, R., Omara, M., Scarpelli, T., Sheng, J., Sulprizio, M. P., Zhuang, J., Zhang, Y., Qu, Z., Lu, X., Hamburg, S. P., and Jacob, D. J.: Unravelling a large methane emission discrepancy in Mexico using satellite observations. Remote Sens. Environ., 260, 112461. https://doi.org/10.1016/j.rse.2021.112461, 2021.

Shen, L., Jacob, D. J., Gautam, R., Omara, M., Scarpelli, T. R., Lorente, A., Zavala-Araiza, D., Lu, X., Chen, Z., and Lin, J.: National quantifications of methane emissions from fuel exploitation using high resolution inversions of satellite observations. Nat. Commun., 14(1), 4948. https://doi.org/10.1038/s41467-023-40671-6, 2023.

Sherwin, E. D., Rutherford, J. S., Zhang, Z., Chen, Y., Wetherley, E. B., Yakovlev, P. V., Berman, E. S. F., Jones, B. B., Cusworth, D. H., Thorpe, A. K., Ayasse, A. K., Duren, R. M., and Brandt, A. R.: US oil and gas system emissions from nearly one million aerial site measurements, Nature, 627, 328–334, https://doi.org/10.1038/s41586-024-07117-5, 2024.

Sierk, B., Fernandez, V., Bézy, J.-L., Meijer, Y., Durand, Y., Bazalgette Courrèges-Lacoste, G., Pachot, C., Löscher, A., Nett, H., Minoglou, K., Boucher, L., Windpassinger, R., Pasquet, A., Serre, D., and Te Hennepe, F.: The Copernicus CO2M mission for monitoring anthropogenic carbon dioxide emissions from space. In Z. Sodnik, B. Cugny, and N. Karafolas (Eds.), International Conference on Space Optics—ICSO 2020 (p. 128). SPIE. https://doi.org/10.1117/12.2599613, 2021.

Staebell, C., Sun, K., Samra, J., Franklin, J., Chan Miller, C., Liu, X., Conway, E., Chance, K., Milligan, S., and Wofsy, S.: Spectral calibration of the MethaneAIR instrument, Atmos. Meas. Tech., 14, https://doi.org/10.5194/amt-14-3737-2021, 2021.

Stell, A. C., Bertolacci, M., Zammit-Mangion, A., Rigby, M., Fraser, P. J., Harth, C. M., Krummel, P. B., Lan, X., Manizza, M., Mühle, J., O'Doherty, S., Prinn, R. G., Weiss, R. F., Young, D., and Ganesan, A. L.: Modelling the growth of atmospheric nitrous oxide using a

https://doi.org/10.5194/egusphere-2026-4693
Preprint. Discussion started: 15 September 2026

global hierarchical inversion, Atmos. Chem. Phys., 22, 12 945–12 960, https://doi.org/10.5194/acp-22-12945-2022, 2022.

Thompson, R. L., and Stohl, A.: FLEXINVERT: An atmospheric Bayesian inversion framework for determining surface fluxes of trace species using an optimized grid. Geosci. Model Dev., 7(5), 2223–2242. https://doi.org/10.5194/gmd-7-2223-2014, 2014.

Thompson, R. L., Stohl, A., Zhou, L. X., Dlugokencky, E., Fukuyama, Y., Tohjima, Y., Kim, S. -Y., Lee, H., Nisbet, E. G., Fisher, R. E., Lowry, D., Weiss, R. F., Prinn, R. G., O'Doherty, S., Young, D., and White, J. W. C.: Methane emissions in East Asia for 2000–2011 estimated using an atmospheric Bayesian inversion. J. Geophys. Res.-Atmos., 120(9), 4352–4369. https://doi.org/10.1002/2014JD022394, 2015.

Thompson, R. L., Krishnankutty, N., Pisso, I., Schneider, P., Stebel, K., Sasakawa, M., Stohl, A., and Platt, S.: Efficient use of a Lagrangian Particle Dispersion Model for atmospheric inversions using satellite observations of column mixing ratios, EGUsphere [preprint], https://doi.org/10.5194/egusphere-2025-147, 2025.

Tomlin, J. M., Lopez-Coto, I., Hajny, K. D., Pitt, J. R., Kaeser, R., Stirm, B. H., Jayarathne, T., Floerchinger, C. R., Commane, R., and Shepson, P. B.: Spatial attribution of aircraft mass balance experiment CO2 estimations for policy-relevant boundaries: New York City. Elem Sci Anth, 11(1), 00046. https://doi.org/10.1525/elementa.2023.00046, 2023.

Subramanian, R., Thompson, R. L., Vojta, M., Schneising, O., and Stohl, A.: Strong monsoon influence on South Asian methane emissions in 2020 revealed by a Bayesian inversion constrained by satellite observations, EGUsphere [preprint], https://doi.org/10.5194/egusphere-2025-5108, 2025.

Varon, D. J., Jacob, D. J., Hmiel, B., Gautam, R., Lyon, D. R., Omara, M., Sulprizio, M., Shen, L., Pendergrass, D., Nesser, H., Qu, Z., Barkley, Z. R., Miles, N. L., Richardson, S. J., Davis, K. J., Pandey, S., Lu, X., Lorente, A., Borsdorff, T., Maasakkers, J. D., and Aben, I.: Continuous weekly monitoring of methane emissions from the Permian Basin by inversion of TROPOMI satellite observations, Atmos. Chem. Phys., 23, 7503–7520, https://doi.org/10.5194/acp-23-7503-2023, 2023.

Varon, D. J., Jacob, D. J., Estrada, L. A., Balasus, N., East, J. D., Pendergrass, D. C., Chen, Z., Sulprizio, M., Omara, M., Gautam, R., Barkley, Z. R., Saldaña, F. J. C., Reidy, E. K., Kamdar, H., Sherwin, E. D., Biraud, S. C., Jervis, D., Pandey, S., Worden, J. R., Bowman, K.,

https://doi.org/10.5194/egusphere-2026-4693
Preprint. Discussion started: 15 September 2026

Maasakkers, J.D., and Kleinberg, R. L.: Seasonality and Declining Intensity of Methane Emissions from the Permian and Nearby US Oil and Gas Basins. Environ. Sci. Technol., 60(1), 425–435. https://doi.org/10.1021/acs.est.5c08745, 2026.

Vaughn, T. L., Bell, C. S., Pickering, C. K., Schwietzke, S., Heath, G. A., Pétron, G., Zimmerle, D. J., Schnell, R. C., and Nummedal, D.: Temporal variability largely explains top-down/bottom-up difference in methane emission estimates from a natural gas production region. Proc. Natl. Acad. Sci. USA, 115(46), 11712–11717. https://doi.org/10.1073/pnas.1805687115, 2018.

Veefkind, J. P., Serrano-Calvo, R., De Gouw, J., Dix, B., Schneising, O., Buchwitz, M., Barré, J., Van Der A, R. J., Liu, M., and Levelt, P. F.: Widespread Frequent Methane Emissions From the Oil and Gas Industry in the Permian Basin. J. Geophys. Res.-Atmos., 128(3), e2022JD037479. https://doi.org/10.1029/2022JD037479, 2023.

Williams, J. P., Omara, M., Himmelberger, A., Zavala-Araiza, D., MacKay, K., Benmergui, J., Sargent, M., Wofsy, S. C., Hamburg, S. P., and Gautam, R.: Small emission sources in aggregate disproportionately account for a large majority of total methane emissions from the US oil and gas sector. Atmos. Chem. Phys., 25(3), 1513–1532. https://doi.org/10.5194/acp-25-1513-2025, 2025.

Williams, J. P., Benmergui, J., Knapp, M., Omara, M., Himmelberger, A., Kyzivat, E., Weatherby, K., Lyke, B., Warren, J., MacKay, K., Ayvazov, S., Russi, M., LoFaso, N., Melendez, T., Miller, C. C., Roche, S., Sargent, M., Franklin, J., Nasr, M., Zhang, Z., Miller, D. J., Luo, B., Guanter, L., Hamburg, S. P., Wofsy, S. C., and Gautam, R.: Methane intensity and emissions across major oil and gas basins and individual jurisdictions using MethaneSAT observations, Atmos. Chem. Phys., 26, 5961–5981, https://doi.org/10.5194/acp-26-5961-2026, 2026.

Zhang, Y., Gautam, R., Pandey, S., Omara, M., Maasakkers, J. D., Sadavarte, P., Lyon, D., Nesser, H., Sulprizio, M. P., Varon, D. J., Zhang, R., Houweling, S., Zavala-Araiza, D., Alvarez, R. A., Lorente, A., Hamburg, S. P., Aben, I., and Jacob, D. J.: Quantifying methane emissions from the largest oil-producing basin in the United States from space. Sci. Adv., 6(17), eaaz5120. https://doi.org/10.1126/sciadv.aaz5120, 2020.

Zhao, Y., Saunois, M., Bousquet, P., Lin, X., Hegglin, M. I., Canadell, J. G., Jackson, R. B., and Zheng, B.: Reconciling the bottom-up and top-down estimates of the methane chemical sink

https://doi.org/10.5194/egusphere-2026-4693
Preprint. Discussion started: 15 September 2026

using multiple observations. Atmos. Chem. Phys., 23(1), 789–807. https://doi.org/10.5194/acp-23-789-2023, 2023.

Zheng, T., Nassar, R., and Baxter, M.: Estimating power plant CO_2 emission using OCO-2 XCO2 and high resolution WRF-Chem simulations, Environ. Res. Lett., 14, 085 001, https://doi.org/10.1088/1748-9326/ab25ae, 2019.